

# One-bit LFM CW Radar: Spectrum Analysis and Target Detection

Benzhou Jin, Jiang Zhu, Qihui Wu, Yuhong Zhang and Zhiwei Xu

## Abstract

One-bit radar involving direct one-bit sampling is a promising technology for many civilian applications due to its low-cost and low-power consumptions. In this paper, problems encountered by one-bit LFM CW radar are studied and a two-stage target detection approach termed as DR-GAMP is proposed. Firstly, the spectrum of one-bit signal in a scenario of multiple targets is analyzed. It is indicated that high-order harmonics may result in false alarms (FAs) and cannot be neglected. Secondly, DR-GAMP is used to suppress the high order harmonics. Specifically, linear preprocessing and predetection are proposed to perform dimension reduction (DR), and then, generalized approximate message passing (GAMP) is utilized to suppress high-order harmonics. Finally, numerical simulations are conducted to evaluate the performance of one-bit LFM CW radar with typical parameters. It is shown that compared to conventional radar with linear processing approach, one-bit LFM CW radar has 0.5 dB performance gain when the input signal-to-noise ratios (SNRs) of targets are low. Moreover, it has 1.6 dB performance loss in a scenario with an additional high SNR target.

**Keywords:** one-bit radar, harmonic suppression, dimension reduction, GAMP, target detection

## I. INTRODUCTION

As radar systems scale up in both bandwidth and the number of antenna elements to improve performances of target detection, recognition and anti-jamming ability [1–4], conventional high-precision analog-to-digital converter (ADC) becomes a limiting factor [5–8] in the fully digital architecture of the modern radar. The fully digital radar has two challenges: (i) Hundreds or even thousands of high-precision ADCs working at Nyquist sampling frequency make the system costly and power-hungry. (ii) The huge data generated by antenna array is difficult to transmit, store, access and process. As a result,

B. Jin and Q. Wu are with the College of Electronic and Information Engineering, Nanjing University of Aeronautics and Astronautics, Nanjing 211106, China. J. Zhu and Z. Xu are with the key laboratory of ocean observation-imaging testbed of Zhejiang Province, Ocean College, Zhejiang University, No.1 Zheda Road, Zhoushan, 316021, China. Y. Zhang is with the School of Electronic Engineering, Xidian University, Xian, Shaanxi 710071, China.

it is unaffordable in practice, especially for civilian applications such as automotive radars and Google's hand gesture recognition radars [9, 10].

A promising solution to overcome the above bottlenecks is to adopt one-bit ADC which has recently attracted considerable research interest for 5G wireless communications systems [11–15] and radar [7, 8, 16–18]. Compared to conventional radar systems, one-bit radar system has two advantages. Firstly, one-bit ADC can be implemented inexpensively and energy efficiently through a simple comparator. Secondly, the data rate generated by antenna array can be largely reduced.

#### A. Related Work

The related signal processing of one-bit radar can be classified into two categories: signal reconstruction based and parameter estimation based methods. From the signal reconstruction point of view, where linear processing approach is usually adopted, the spectrum of one-bit quantized signals, sampling frequency and target detection methods have been studied [8, 17–22]. While from the parameter estimation point of view, the goal is to perform target detection and localization directly via nonlinear processing such as compressed sensing algorithms. Both the nonlinear signal processing methods [7, 16, 23] and the effect of oversampling [24–27] have been studied.

1) *Signal Reconstruction*: In [19], the spectrum of one-bit quantized sinusoidal signal is analyzed and synthetic aperture radar (SAR) imaging is considered. Results show that the quantized signal consists of plentiful self-generated high-order harmonics. When the SNR is low, conventional linear method, e.g., matched filtering, can still be used for SAR imaging and the performance degradation is small. In contrast, this work focus on target detection and extends [19]. The spectrum of cross-generated harmonics caused by one-bit quantization is analyzed. In [20, 21], the effects of high-order harmonics on SAR imaging performance are studied when strong scatters with high SNRs are present in the received signals. For high SNR scenarios, high-order harmonics can not neglected and will enlarge the bandwidth of the received signal. From the respect of linear signal processing, oversampling reduce the overlap between the spectrum of fundamental components and high-order harmonics [21], and is beneficial for SAR imaging. It is shown that the aliasing effect caused by high-order harmonics can be reduced effectively with an oversampling being 2. In [8], in order to suppress high-order harmonics and perform target detection based the one-bit samples efficiently using conventional algorithms, an unknown dithering scheme is proposed for linear frequency modulated continuous wave (LFMCW) radar. However, adding noise reduces the received target SNRs simultaneously and hence results in performance degradation for target detection.

2) *Parameter Estimation*: In [7], target detection of one-bit pulse radar in fast time domain is studied, and a  $l_1$  minimization based sparse target detection approach is proposed. Numerical results demonstrate

the effectiveness of the proposed approach. In [16], the spatial domain is taken into account and target detection is carried out in fast time domain for each antenna element. In [23], A maximum a posteriori (MAP) approach is proposed for one-bit SAR imaging. Compared to the above works, this paper takes all of three domains, i.e., spatial, slow time, and fast time domain into account. When all of three domains are considered, the dimension of the observation model is generally huge and the previous methods can not be applied directly. While in this work, a two-stage DR-GAMP approach is proposed to perform target detection and localization. As for sampling frequency, the loss caused by one-bit ADC can be compensated by oversampling as well. It is shown that Nyquist rate results in performance loss more than  $2/\pi$  (for low SNR case, the loss is about  $2/\pi$ ) compared to unquantized system, oversampling can reduce this performance loss [25].

### *B. Contributions*

This paper studies the one-bit LFM CW radar system. All of the three dimensional signal processing i.e., spatial, slow time, and fast time domain are taken into account. The main contributions of this work can be summarized as follows:

- The spectrum of one-bit signal is analyzed. In particular, for a two targets scenario, the closed-form of the average amplitudes of the cross-generated harmonics are obtained. The average amplitudes of the 3-order cross-generated harmonics are larger than that of the 3-order self-generated harmonics if the two targets have the same received SNRs, i.e.,  $\text{SNR}_1 = \text{SNR}_2$ . Moreover, it is shown that the 3-order harmonics can cause FAs.
- To suppress the harmonics, a two-stage approach DR-GAMP exploiting the sparsity of the targets in the searching space is proposed. In the first stage, conventional linear processing methods are implemented to perform dimension reduction (DR). In the second stage, GAMP algorithm is adopted to suppress the harmonics and recover true targets. It is numerically shown that DR-GAMP benefits significantly from DR.
- Performances of the proposed method are investigated for both on-gird and off-gird cases through numerical simulations under typical parameters. Results show that DR-GAMP is effective to remove high-order harmonic FAs and perform target detection for one-bit LFM CW radar.

The rest of this paper is organized as follows. In Section II, signal model is introduced. The spectrum of one-bit signal and its effects on target detection are analyzed in Section III. Then the proposed DR-GAMP is presented in Section IV. In Section V, substantial numerical experiments are conducted to illustrate the performance of one-bit LFM CW radar. Finally, we conclude the paper in Section VI.

### C. Notation

Let  $\text{csign}(\cdot) = \text{sign}(\text{Re}(\cdot)) + j\text{sign}(\text{Im}(\cdot))$ , where  $\text{Re}(\cdot)$  and  $\text{Im}(\cdot)$  denote the real and imaginary parts, respectively, and  $\text{sign}(\cdot)$  returns the componentwise sign. Let  $\mathbb{E}(\cdot)$  denote the expectation operation. Let  $\otimes$  denote the Kronecker product.  $\mathcal{F}(\cdot)$  denotes the Fourier transform.  $\|\cdot\|_0$  is the zero pseudo-norm.  $\lfloor \cdot \rfloor$  rounds its variable to the nearest integer less than or equal to that variable.  $\text{rect}(\cdot)$  denotes the rectangle function.

## II. SIGNAL MODEL

In this paper, the transmitter for one-bit LFMCW radar is the same as the conventional radar and in a coherent pulse interval (CPI), periodic linear frequency modulated pulses are transmitted. Considering a fully digital uniform linear array, the receiver architecture and general model of data collection for one-bit LFMCW radar is illustrated in Fig. 1. Different from conventional radar applying high-precision ADCs, one-bit ADCs are adopted.

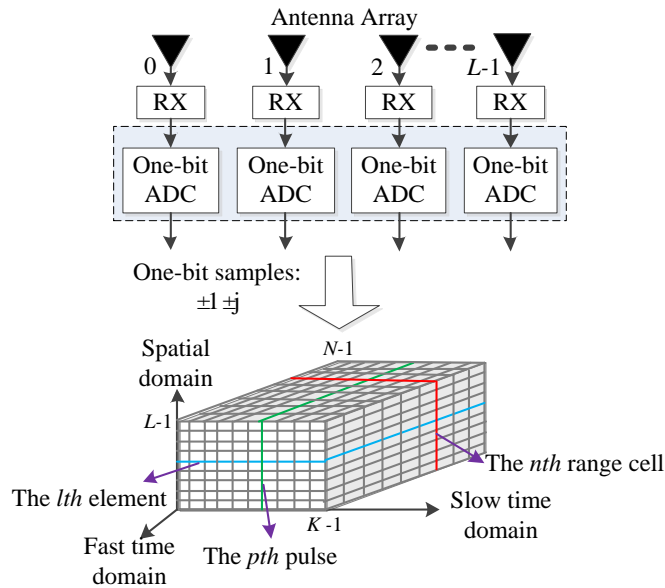


Fig. 1. The receiver architecture and general model of data collection for a fully digital one-bit radar. RX denotes the RF channel mainly including low noise amplifier (LNA), dechirping and filter. After RX, one-bit ADC is applied to implement signal sampling. After sampling, the baseband data can be collected in a data cube.

As shown in Fig. 1, each antenna element includes a separate radio frequency (RF) channel represented as the RX block. Before dechirping (also known as stretch processing), the received signal in a CPI for

the  $l$ th antenna element can be represented as <sup>1</sup>

$$q_l(t) = \sum_{p=1}^P \tilde{\sigma}_{s,p} \text{rect}\left(\frac{t - kT_I - \tau_p(t)}{T_I}\right) \exp(-j2\pi f_c(t - kT_I - \tau_p(t)) + j\pi\mu(t - kT_I - \tau_p(t))^2 + j2\pi f_{sp,p}l) + w_q(t), \quad (0 \leq t \leq (K-1)T_I) \quad (1)$$

where  $0 \leq l \leq L-1$ ,  $f_c$  is the carrier frequency,  $P$  is the number of targets,  $\tau_p(t)$  is the delay of the  $p$ th target and  $\tilde{\sigma}_{s,p}$  is the random, complex voltage.  $K$  is the number of pulses in a CPI,  $0 \leq k \leq K-1$ .  $T_I$  is the pulse interval and  $\mu$  is the frequency modulation slope.  $w_q(t)$  is the additive white Gaussian noise (AWGN).  $f_{sp,p} = d \sin \varphi_p / \lambda$  is the spatial frequency, where  $\varphi_p$  is the azimuth angle of the  $p$ th target and  $d$  is the inter-element spacing of the antenna array. Then, the dechirping is performed to obtain a beat signal as

$$r_l(t) = q_l(t) \text{rect}\left(\frac{t - kT_I}{T_I}\right) \exp(j2\pi f_c(t - kT_I) - j\pi\mu(t - kT_I)^2). \quad (2)$$

Let  $\tau_{\max}$  be the maximum target delay and  $0 < \tau_p(t) \leq \tau_{\max}$ . The valid observation time in the  $k$ th pulse is  $(kT_I + \tau_{\max}, (k+1)T_I]$ . Here, we merely consider the received signal (2) in the valid time duration and we have

$$r_l(t) = \sum_{p=1}^P \tilde{\sigma}_{s,p} \exp(-j2\pi f_c \tau_p(t) - j2\pi\mu(t - kT_I)\tau_p(t) + j\pi\mu\tau_p^2(t) + j2\pi f_{sp,p}l) + w_q(t), \quad (3)$$

where  $\tau_p(t)$  is  $\tau_p(t) = 2(R_{0,p} - v_p t) / c = \tau_{0,p} - 2v_p(kT_I + t - kT_I) / c$ ,  $R_{0,p}$  is the initial range of the  $p$ th target for the current CPI,  $\tau_{0,p} = 2R_{0,p} / c$  and  $c$  is the speed of light.  $kT_I$  and  $t - kT_I$  are known as the slow time and fast time, respectively. Then, (3) can be further simplified as

$$r_l(t) = \sum_{p=1}^P \sigma_{s,p} \exp\left(j2\pi(f_{d,p}kT_I + (f_{r,p} + f_{d,p} + 2\mu v_p t / c)(t - kT_I) + f_{sp,p}l + \frac{1}{2}\mu\tau_p^2(t))\right) + w_q(t), \quad (4)$$

where  $\sigma_{s,p} = \tilde{\sigma}_{s,p} \exp(-j4\pi R_{0,p} / \lambda)$ ,  $f_{d,p} = 2v_p / \lambda$  is the Doppler shift,  $v_p$  denotes the  $p$ th target velocity.  $f_{r,p} = -\mu\tau_{0,p}$  denotes beat frequency which represents the range of the  $p$ th target. In general,  $|(f_{d,p} + 2\mu v_p t / c)(t - kT_I)| \ll 1$  and  $|\mu\tau_p^2(t)| \ll 1$ . Hence, (4) can be approximated as

$$r_l(t) \approx \sum_{p=1}^P \sigma_{s,p} \exp(j2\pi(f_{d,p}kT_I + f_{r,p}(t - kT_I) + f_{sp,p}l)) + w(t), \quad (5)$$

The signal bandwidth of targets in the fast time domain is no more than  $|\mu\tau_{\max}|$ , i.e.,  $f_{r,p} \in [-B_r, 0]$ . Then, the received signal bandwidth is limited to  $B_r$  by applying a bandpass filter. Meanwhile, the

<sup>1</sup>Here the clutter are neglected. Since the clutter can be modeled as a signal dependent noise and is correlated over the slow time domain, it is difficult to analyze the performance and provide effective detection algorithms. This paper plans to take a first step to study the one-bit LFM CW radar without clutter.

bandwidth of noise is reduced to  $B_r$  as well. After one-bit ADC sampling, the received data in one CPI can be represented by a  $K \times L \times N$  data cube, as shown in Fig. 1. The one-bit baseband sample  $r(k, l, n)$  of the data cube can be modeled as

$$r(k, l, n) = \text{csign} \left( \sum_{p=1}^P \sigma_{s,p} \exp(j2\pi(f_{r,p}nT_s + f_{d,p}kT_I + f_{sp,p}l)) + w(k, l, n) \right), \quad (6)$$

where  $0 \leq n \leq N - 1$  and  $N$  is the number of samples in the fast time domain within the duration  $T$  in one received pulse.  $T_s = 1/f_s$  is the sampling interval.

For conventional system with high-precision ADCs, linear signal processing is generally implemented independently in the three domains. In contrast, as will be seen, the nonlinear algorithm is applied to process the received data in the three domains jointly in one-bit radar system. In order to satisfy the later requirement of one-bit signal processing, we subsequently represent the received signal model in matrix forms.

The slow time domain is first considered. The continuous Doppler shifts of targets lie in the interval  $[0, \text{PRF}]$ , where  $\text{PRF} = 1/T_I$  denotes the pulse repetition frequency (PRF). Here, this interval is discretized into  $M_d$  grids and in order to establish the signal model, we assume that the Doppler shifts of targets lie on the grid. In general,  $M_d$  should satisfies  $(\text{PRF}/M_d) \leq \Delta f_d$ , i.e.,  $M_d \geq K$ , where  $\Delta f_d = 1/(KT_I)$  denotes the Doppler frequency resolution. We construct a dictionary matrix  $\mathbf{A}_d \in \mathbb{C}^{K \times M_d}$  whose  $m_d$ th column is  $\mathbf{a}_d(f_{d,m_d}) = [1, \exp(j2\pi f_{d,m_d}T_I), \dots, \exp(j2\pi(K-1)f_{d,m_d}T_I)]^T$ , where  $0 \leq m_d \leq M_d - 1$  denotes slow time grid index and  $f_{d,m_d} = (m_d \text{PRF})/M_d$ . Then, for the  $l$ th antenna element and  $n$ th range cell, the received signal can be expressed as

$$\mathbf{r}_d(l, n) = \text{csign} (\mathbf{A}_d \mathbf{x}_d(l, n) + \mathbf{w}_d(l, n)), \quad (7)$$

where  $\mathbf{x}_d(l, n) = [x_{d,0}(l, n), \dots, x_{d,m_d}(l, n), \dots, x_{d,M_d-1}(l, n)]^T \in \mathbb{C}^{M_d \times 1}$  and the number of nonzero element of  $\mathbf{x}_d(l, n)$  satisfies  $\|\mathbf{x}_d(l, n)\|_0 \leq P$ . The inequality comes from the fact that targets with different spatial or beat frequency may share the same Doppler shift, otherwise equality holds. In practice, targets do not lie on the grids exactly. However, when the dictionary is densely enough, (7) is valid and  $\mathbf{x}_d(l, n)$  is approximately sparse [28].

Similarly, observation vectors in the spatial and fast time domain can be described by

$$\mathbf{r}_{sp}(k, n) = \text{csign} (\mathbf{A}_{sp} \mathbf{x}_{sp}(k, n) + \mathbf{w}_{sp}(k, n)), \quad (8)$$

and

$$\mathbf{r}_r(k, l) = \text{csign} (\mathbf{A}_r \mathbf{x}_r(k, l) + \mathbf{w}_r(k, l)), \quad (9)$$

where  $\mathbf{x}_{sp}(k, n) = [x_{sp,0}(k, n), \dots, x_{sp,m_{sp}}(k, n), \dots, x_{sp,M_{sp}-1}(k, n)]^T \in \mathbb{C}^{M_{sp} \times 1}$  and  $M_{sp}$  denotes the number of grids in spatial domain.  $\mathbf{x}_r(k, l) = [x_{r,0}(k, l), \dots, x_{r,m_r}(k, l), \dots, x_{r,M_r-1}(k, l)]^T \in \mathbb{C}^{M_r \times 1}$  and  $M_r$  denotes the number of grids in fast time domain.  $m_{sp}$  and  $m_r$  are the spatial and fast time grid indices, respectively. Generally,  $M_{sp} \geq L$  and  $M_r \geq N$ . We assume the spatial frequencies and beat frequencies of targets lie on the grid as well. Similar to the case in the slow time domain, the number of nonzero elements of  $\mathbf{x}_{sp}(k, n)$  and  $\mathbf{x}_r(k, l)$  satisfy  $\|\mathbf{x}_{sp}(k, n)\|_0 \leq P$  and  $\|\mathbf{x}_r(k, l)\|_0 \leq P$ , respectively. At  $m_{sp}$ th spatial grid, the spatial frequency is  $f_{sp,m_{sp}} = m_{sp}/L$ . For the fast time domain, the beat frequency at  $m_r$ th grid is  $f_{r,m_r} = -2\mu R_{m_r}/c$ , where  $R_{m_r}$  is the target range corresponding to the  $m_r$ th grid.  $\mathbf{A}_{sp} \in \mathbb{C}^{L \times M_{sp}}$  is the dictionary matrix in the spatial domain and its  $m_{sp}$ th column is  $\mathbf{a}_{sp}(f_{sp,m_{sp}}) = [1, \exp(j2\pi f_{sp,m_{sp}}), \dots, \exp(j2\pi(L-1)f_{sp,m_{sp}})]^T$ .  $\mathbf{A}_r$  is the dictionary matrix in the fast time domain and its  $m_r$ th column is  $\mathbf{a}_r(f_{r,m_r}) = [1, \exp(j2\pi f_{r,m_r}), \dots, \exp(j2\pi(N-1)f_{r,m_r})]^T$ .

Combining (7), (8) and (9), the received data cube can be reduced to a  $KLN \times 1$  column vector which is represented as

$$\mathbf{r} = \text{csign}(\mathbf{A}\mathbf{x} + \mathbf{w}), \quad (10)$$

$\mathbf{x} = [x(0), \dots, x(m_d M_{sp} M_r + m_{sp} M_r + m_r), \dots, x(M_d M_{sp} M_r - 1)]^T \in \mathbb{C}^{M_d M_{sp} M_r \times 1}$  and  $x(m_d(M_{sp} M_r) + m_{sp} M_r + m_r)$  denotes the complex amplitude of the target whose Doppler shift, spatial frequency and beat frequency are  $f_{d,m_d}$ ,  $f_{sp,m_{sp}}$  and  $f_{r,m_r}$ , respectively.  $\mathbf{A} = \mathbf{A}_d \otimes \mathbf{A}_{sp} \otimes \mathbf{A}_r \in \mathbb{C}^{LKN \times M_d M_{sp} M_r}$ . In the three signal domain, targets are generally sparse and typically, the number of nonzero elements of  $\mathbf{x}$  satisfies  $\|\mathbf{x}\|_0 = P \ll M_d M_{sp} M_r$ .

Because one-bit ADC is a highly nonlinear device, conventional linear processing methods, as shown in the ensuing Section III, may be ineffective because of harmonics. While for nonlinear reconstruction methods, it is generally impossible to implement because of the large dimension of  $\mathbf{A}$  in (10). For example, assuming the vector  $\mathbf{r}$  and  $\mathbf{x}$  both have dimension  $10^6$ , the matrix  $\mathbf{A}$  contains  $10^{12}$  entries which leads to difficulties with computation and memory.

### III. SPECTRUM ANALYSIS OF ONE-BIT QUANTIZED SIGNAL

For the target detection in one-bit radar, a natural question is whether linear processing methods, e.g., fast Fourier transform (FFT), are still effective or not. To answer this question, signal spectrum of one-bit signal is investigated in a multiple target scenarios. An approximation of one-bit signal after FFT is provided based on which, effects of one-bit quantization on target detection are discussed.

### A. Harmonics analysis

In this subsection, the real part of the received complex one-bit signal is firstly analyzed and then the main difference between the real signal and complex signal is provided. Without loss of generality, we take the signal in fast time domain of (6) for example to analyze. In the continuous form, according to (6) with both indices of the slow time and spatial domain fixed, the received signal of one pulse in the fast time domain can be abstracted as

$$v_q(t) = \text{rect}\left(\frac{t}{T}\right) \text{sign}\left(\sum_{p=1}^P A_p \cos(\omega_p t + \Phi_p) + w(t)\right) \quad (11)$$

Since the term  $\text{rect}\left(\frac{t}{T}\right)$  has no effect on the discuss of harmonic characteristics and its effects on spectrum of  $v_q(t)$  is known, we ignore  $\text{rect}\left(\frac{t}{T}\right)$  in the following for simplicity. Let  $u(t) = \sum_{p=1}^P A_p \cos(\omega_p t + \Phi_p)$ , the one-bit signal  $v_q(t)$  is given by

$$\begin{aligned} v_q(t) &= \text{sign}(u + w) = -\frac{j}{\pi} \int_{-\infty}^{\infty} \frac{\exp(j(u + w)\xi)}{\xi} d\xi \\ &= -\frac{j}{\pi} \int_{-\infty}^{\infty} \frac{\exp(jw\xi)}{\xi} \left( \prod_{p=1}^P e^{jA_p \cos(\omega_p t + \Phi_p)\xi} \right) d\xi \\ &\stackrel{(a)}{=} -\frac{j}{\pi} \int_{-\infty}^{\infty} \frac{\exp(jw\xi)}{\xi} \prod_{p=1}^P \left( \sum_{m_p=0}^{\infty} \epsilon_{m_p} j^{m_p} J_{m_p}(A_p \xi) \cos(m_p \omega_p t + m_p \Phi_p) \right) d\xi, \end{aligned} \quad (12)$$

where  $J_{m_p}(\cdot)$  is the Bessel function of the first kind and equality (a) follows from [29, pp. 361].  $\epsilon_0 = 1$  and  $\epsilon_m = 2$  for  $m \geq 1$ . From equation (12), it is shown that  $v_q(t)$  not only preserves their original frequencies (also known as fundamental harmonics), but also generates new frequencies (higher-order harmonics) due to both the cross terms of the original different sinusoidal signals and terms of the same sinusoidal signals. Amplitudes of both original and new frequencies in  $v_q(t)$  are related to the noise  $w(t)$ , i.e. these amplitudes are all random variables. As will be seen in section IV, one-bit signal is first processed using 3-D FFT in the slow time, spatial, and fast time domain. Clearly, the 3-D FFT can be regarded as an averaging process over the noise signal  $w(t)$ . Since the number of observation points is very large in radar, similar to [19], amplitudes of both original and new frequencies can be represented approximately by its average value after 3-D FFT. The average of  $v_q(t)$  with respect to  $w(t)$  is

$$\begin{aligned} E(v_q(t)) &= -\frac{j}{\pi} \int_{-\infty}^{\infty} \frac{1}{\sqrt{2\pi\sigma_w^2}} e^{-\frac{w^2}{2\sigma_w^2}} \int_{-\infty}^{\infty} \frac{e^{jw\xi}}{\xi} \prod_{p=1}^P \left( \sum_{m_p=0}^{\infty} \epsilon_{m_p} j^{m_p} J_{m_p}(A_p \xi) \cos(m_p \omega_p t + m_p \Phi_p) \right) dw d\xi \\ &= -\frac{j}{\pi} \int_{-\infty}^{\infty} \frac{e^{-\frac{\sigma_w^2 \xi^2}{2}}}{\xi} \prod_{p=1}^P \left( \sum_{m_p=0}^{\infty} \epsilon_{m_p} j^{m_p} J_{m_p}(A_p \xi) \cos(m_p \omega_p t + m_p \Phi_p) \right) d\xi, \end{aligned} \quad (13)$$



where the expectation  $E(\cdot)$  is taken with respect to the noise  $w$  and  $\sigma_w^2$  is the noise power. From equation (13), the self-generated and cross-generated harmonics can be extracted. For an even  $m$ , i.e.,  $m = m_1 + \dots + m_P$  is an even nonnegative number including zero, both the average amplitudes of self-generated and cross-generated harmonics are equal to zero (refer to Appendix VII-A). For an odd  $m$ , calculating the average amplitudes of the harmonics is rather clumsy and not necessary for a general  $P$ . In [19], the spectrum under  $P = 1$  has been analyzed. For completeness, we outline the results presented in [19]. To reveal the characteristics of both self-generated and cross-generated harmonics, the spectrum under  $P = 2$  are studied. Detailed derivations are moved to Appendix VII-A and here, we summarize the main results and provide interesting insights.

For  $P = 1$ , the average signal  $E(v_q(t))$  is [19]

$$E(v_q(t)) = \sum_{m=1, m \text{ odd}}^{\infty} c_m \cos(m\omega t + m\Phi), \quad (14)$$

where

$$c_m = -j^{m+1} \sqrt{\frac{2}{\pi}} \alpha_m \left( \frac{A_1}{\sigma_w} \right)^m F\left(\frac{m}{2}; m+1; -\frac{A_1^2}{2\sigma_w^2}\right), \quad (15)$$

$F\left(\frac{m}{2}; m+1; -\frac{A_1^2}{2\sigma_w^2}\right)$  is the hypergeometric function [29, pp. 504],

$$\alpha_m = \frac{1}{\left(\frac{m-1}{2}\right)! m} 2^{-\frac{3(m-1)}{2}}, \quad m \text{ is odd.} \quad (16)$$

For example,  $\alpha_1 = 1$ ,  $\alpha_3 = 1/24$ ,  $\alpha_5 = 1/640$ . When the received SNR =  $10\log(A_1^2/2\sigma_w^2) \ll 0$  dB,  $F(\cdot, \cdot, \cdot) \approx 1$ , for a nonnegative integer value  $m$  we have

$$|c_m| \approx \sqrt{\frac{2}{\pi}} \alpha_m \left( \frac{A_1}{\sigma_w} \right)^m. \quad (17)$$

According to (17), we have

$$20 \log \frac{|c_m|}{|c_1|} \approx 20(m-1) \log \frac{A_1}{\sigma_w} + 20 \log \frac{\alpha_m}{\alpha_1}. \quad (18)$$

When SNR  $\ll 0$  dB, the harmonics decrease rapidly with the harmonic order  $m$ . Nevertheless, whether high-order harmonics can be omitted or not is determined by the following three factors: the received SNR, the order  $m$  and the digital integration gain of radar. As will be seen later, the 3-order harmonic can not be omitted for many applications. For  $m > 5$ , the average energy of harmonics are really small and can be omitted. For the case  $m = 5$ , 5-order harmonics are merely needed to be considered in some cases at high received SNRs.

For  $P = 2$ , the average signal  $E(v_q(t))$  can be viewed as the superposition of the self-generated harmonics and cross-generated harmonics (Note that for  $P = 1$ , the average signal  $E(v_q(t))$  only has self-generated harmonics.). The general expression for the average amplitudes of the self-generated and

cross-generated harmonics are given in (41) and (43) (refer to Appendix VII-A). Here we consider the special case where  $A_1 = A_2$  and reveal characteristics about the self-generated and cross-generated harmonics.

For the  $m$ -order self-generated harmonics, without loss of generality, we only consider the coefficient of  $c_{m,0} \cos(m\omega_1 t + m\Phi_1)$  from the first target signal  $A_1 \cos(\omega_1 t + \Phi_1)$ . From (41) in Appendix VII-A, the coefficient is given by

$$c_{m,0} = -j^{m+1} \sqrt{\frac{2}{\pi}} \frac{1}{\left(\frac{m-1}{2}\right)! m} 2^{-\frac{3(m-1)}{2}} {}_3F_3 \left( \frac{m+1}{2}, \frac{m}{2} + 1, \frac{m}{2}; 1, m+1, m+1; -\frac{2A_2^2}{\sigma_w^2} \right). \quad (19)$$

When  $\text{SNR} \ll 0$  dB,  $F(\cdot, \cdot, \cdot) \approx 1$  and we have

$$|c_{m,0}| \approx \sqrt{\frac{2}{\pi}} \alpha_m \left( \frac{A_1}{\sigma_w} \right)^m. \quad (20)$$

The above result is the same as the  $P = 1$  case as shown in (17).

For the  $m$ -order cross-generated term  $c_{m_1, m_2} \cos(m_2 \omega_2 t + m_2 \Phi_2) \cos(m_1 \omega_1 t + m_1 \Phi_1)$ , if  $A_1 = A_2$ , the coefficient  $c_{m_1, m_2}$  is calculated by (refer to (43) in Appendix VII-A)

$$c_{m_1, m_2} = -j^{m+1} \sqrt{\frac{2}{\pi}} 2^{-m+2} \frac{(m-2)!!}{m_1! m_2!} \left( \frac{A_1}{\sigma_w} \right)^m {}_3F_3 \left( \frac{m+1}{2}, \frac{m}{2} + 1, \frac{m}{2}; m_2 + 1, m_1 + 1, m + 1; -\frac{2A_2^2}{\sigma_w^2} \right). \quad (21)$$

where  $(m-2)!! = 1 \times 3 \times 5 \cdots \times (m-2)$  and  $m = m_1 + m_2$ .

When  $\text{SNR} \ll 0$  dB, we have

$$c_{m_1, m_2} \approx -j^{m+1} \sqrt{\frac{2}{\pi}} \alpha'_{m_1, m_2} \left( \frac{A_1}{\sigma_w} \right)^m, \quad (22)$$

where

$$\alpha'_{m_1, m_2} = 2^{-m+2} \frac{(m-2)!!}{m_1! m_2!}. \quad (23)$$

Consider the 3-order self-generated and cross-generated harmonics, according to (20) and (22), we have

$$20 \log \frac{\alpha'_{1,2}/2}{c_{3,0}} = 20 \log 3 \approx 9.5 \text{ dB}. \quad (24)$$

In (24), it shows that for the  $A_1 = A_2$  case, the average energy of the 3-order cross-generated harmonics is 9.5 dB higher than that of the 3-order self-generated harmonics. As a result, the 3-order cross-generated harmonics may have a stronger effect on target detection in practice.

Subsequently, we consider a complex signal. In a single target scenario, the complex signal after one-bit quantization is

$$u_C(t) = \text{csign} \left( A_1 e^{j(\omega t + \Phi)} \right) = \text{sign} \left( A_1 \cos(\omega t + \Phi) \right) + j \left( \text{sign} A_1 \cos(\omega t + \Phi - \pi/2) \right). \quad (25)$$

Its spectrum can be, respectively, obtained through analyzing the real and imaginary parts and similar results can be obtained. Comparing with real signal, we need to pay attention to the frequency localizations of high-order harmonics. For example, according to (14) and (25), the 3-order harmonic is

$$c_3 \cos(3\omega t + 3\Phi) + jc_3 \cos(3\omega t + 3\Phi - 3\pi/2) = c_3 e^{-j(3\omega t + 3\Phi)}, \quad (26)$$

which means that the frequency of the self-generated 3-harmonic is  $-3\omega$ . Furthermore, when the number of targets is  $P = 2$ , it can be calculated that the 3-order harmonics contain 6 components and the corresponding frequencies are  $-3w_1, -3w_2, 2w_1 - w_2, 2w_2 - w_1, -2w_1 - w_2$ , and  $-2w_2 - w_1$ , respectively. For a general  $P$  and the order  $m$ , we can similarly obtain the frequency localizations.

### B. Approximation of one-bit signal after FFT

We still take the signal in fast time domain for example and omit  $\text{rect}(\frac{t}{T})$ . The received one-bit complex signal in continuous form can be described as

$$v_{qC}(t) = \text{csign} \left( \sum_{p=1}^P A_p \exp(j(w_p t + \Phi_p)) + w(t) \right). \quad (27)$$

For the  $p$ th target, its received SNR before one-bit quantization is defined as  $\text{SNR}_p = 10 \log(|A_p|^2 / (2\sigma_w^2))$ , where  $\sigma_w^2$  is the noise power of the real part or image part of  $v_{qC}(t)$ .

For many applications,  $\text{SNR}_p$  satisfies  $\text{SNR}_p < 0$  dB and then,  $m$ -order harmonics ( $m > 5$ ) can be generally neglected since their average amplitudes are really small. The average of  $\mathcal{F}(v_{qC}(t))$  can be approximated as

$$\text{E}(\mathcal{F}(v_{qC}(t))) \approx \sum_{q=1}^Q A_q \delta(f - f_q), \quad (28)$$

where  $Q$  is the number of main components in (27) including fundamental and 3/5-order harmonics.

Similar to [19] and the previous analysis in (13), the signal component (including harmonics) of  $v_{qC}(t)$  can be represented approximately by their average value after Fourier transform. Taking the noise into account, we have

$$\mathcal{F}(v_{qC}(t)) \approx \text{E}(\mathcal{F}(v_{qC}(t))) + w(f). \quad (29)$$

Here, we assume the term  $w(f)$  is Gaussian noise with its bandwidth  $B_r$ . Such an assumption will be validated through numerical experiments in Section V. Using the approximation (28), (29), the one-bit signal after performing the Fourier transform can be approximated as

$$\mathcal{F}(v_{qC}(t)) \approx \sum_{q=1}^Q A_q \delta(f - f_q) + w(f). \quad (30)$$

The above assumption shows the following two important points:

- 1) When the signal (27) is sampled, the conventional FFT processing method is still effective for improving the SNR of both fundamental and high-order harmonics.
- 2) Based on the FFT results, we can design the CFAR detector to detect both fundamental and high-order harmonics. The fundamental components correspond to true targets, while high-order harmonics detected are called as ghost targets or FAs that need to suppress.

#### IV. A TWO-STAGE DR-GAMP TARGET DETECTION APPROACH

Section III shows that for one-bit signal in (6), linear approach is effective for improving target SNRs, while it is difficult to suppress higher-order harmonics. To overcome the drawback, GAMP algorithm which takes the quantization effects into account is proposed. Nevertheless, because the number of grids in the target space is very large in a typical radar system, considering the computation and memory required, GAMP can not be performed directly. As a result, a two-stage DR-GAMP target detection scheme is proposed and is shown in Fig. 2. At the first stage, efficient linear processing is applied in the three domains separately to improve target SNRs and then a pre-detection procedure is carried out to perform DR. At the second stage, GAMP algorithm is performed to recover the true targets and suppresses the harmonics simultaneously.

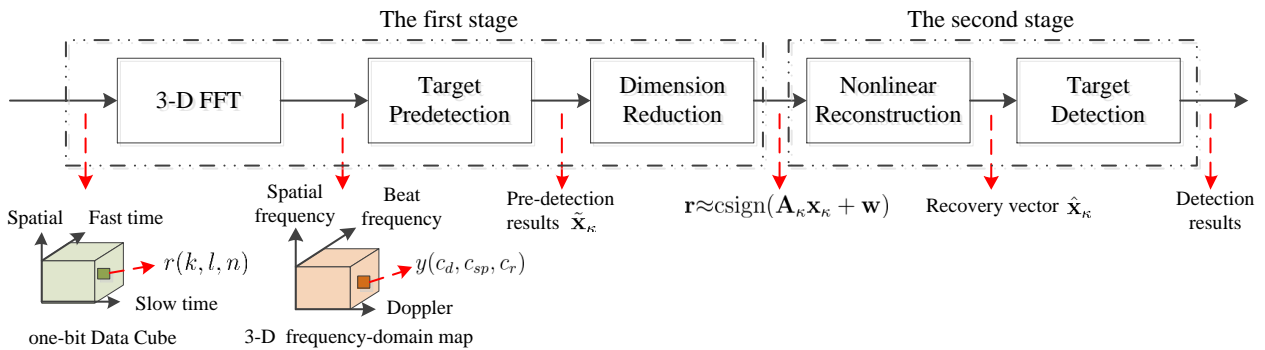


Fig. 2. A two-stage DR-GAMP target detection scheme. In the first stage, linear processing is applied to perform DR. In the second stage, GAMP is adopted firstly to suppress FAs and then, target detection is carried out based on reconstruction results of GAMP.

##### A. Dimension Reduction

3-D FFT is firstly performed over the slow time, spatial, and fast time domain of the received one-bit data cube, respectively. By 3-D FFT procedures, the SNRs of the fundamental frequencies and high-order

harmonics of one-bit signal can be all integrated coherently. Assuming the FFT points in the slow time, spatial, and fast time domain are  $C_d$ ,  $C_{sp}$  and  $C_r$ , the element of the output 3-D frequency-domain map can be represented as

$$y(c_d, c_{sp}, c_r) = \mathbf{a}^H(c_d, c_{sp}, c_r) \mathbf{r}, \quad 0 \leq c_d \leq C_d - 1, 0 \leq c_{sp} \leq C_{sp} - 1, 0 \leq c_r \leq C_r - 1. \quad (31)$$

where  $\mathbf{r}$  is the received data in vector form, as shown in (10).  $\mathbf{a}(c_d, c_{sp}, c_r)$  is the steering vector of the current cell in frequency domain and

$$\mathbf{a}(c_d, c_{sp}, c_r) = \mathbf{a}_d(f_{d,c_d}) \otimes \mathbf{a}_{sp}(f_{sp,c_{sp}}) \otimes \mathbf{a}_r(f_{r,c_r}), \quad (32)$$

where  $f_{d,c_d}$ ,  $f_{sp,c_{sp}}$  and  $f_{r,c_r}$  denotes the Doppler, spatial and beat frequency, respectively, and  $f_{d,c_d} = (c_d \text{PRF})/C_d$ ,  $f_{sp,c_{sp}} = c_{sp}/C_{sp}$  and  $f_{r,c_r} = (c_r f_s)/C_r$ .

Subsequently, target predetection is implemented for the 3-D frequency-domain map. In this paper, we apply the order statistic constant false alarm rate (OS CFAR) detector [30, pp. 371]. The threshold  $\gamma_1$  of the OS CFAR detector is

$$\gamma_1 = \alpha_{OS} x_\eta, \quad (33)$$

where  $x_\eta$  is the  $\eta$ th order statistic of reference cells,  $\alpha_{OS}$  is a scale factor. OS CFAR is sequentially performed over the Doppler, spatial and beat frequency domain, respectively. Let  $I_{pd}$  denote the number of pre-detection targets (PTs) after OS CFAR. PTs consist of three parts, i.e., true targets, FAs caused by the high-order harmonics and FAs caused by noise.  $\gamma_1$  is chosen based on the noise FAs rate  $P_{FA,w}$ . Under the assumption of Gaussian noise in (30),  $\gamma_1$  can be easily set based on  $P_{FA,w}$ . Typically, we can set a very small  $P_{FA,w}$ , e.g., ranging from  $P_{FA,w} = 10^{-3} \sim 10^{-6}$ . On the other hand, for most practical scenarios, true targets and their  $m$ -order harmonics (consider  $m \leq 5$  case) are sparse in the 3-D frequency data cube as well. That is the FA rate  $P_{FA,h}$  caused by high-order harmonics satisfies  $P_{FA,h} \ll 1$  as well. Therefore,  $I_{pd}$  obviously satisfies  $I_{pd} \ll C_d C_{sp} C_r$ . Let  $\tilde{\mathbf{x}}_\kappa = [\tilde{x}_\kappa(0), \dots, \tilde{x}_\kappa(i_{pd}), \dots, \tilde{x}_\kappa(I_{pd} - 1)]^T \in \mathbb{C}^{I_{pd} \times 1}$  represents the pre-detection vector, where  $\tilde{x}_\kappa(i_{pd})$  denotes the complex amplitude of the  $i_{pd}$ th PT and its corresponding frequency cell indices are  $c_{d,i_{pd}}$ ,  $c_{sp,i_{pd}}$  and  $c_{r,i_{pd}}$ , respectively, and  $0 \leq c_{d,i_{pd}} \leq C_d - 1$ ,  $0 \leq c_{sp,i_{pd}} \leq C_{sp}$  and  $0 \leq c_{r,i_{pd}} \leq C_r$ .

Considering the definition of  $m_d$ ,  $m_{sp}$  and  $m_r$ , the frequency cell indices of  $c_d$ ,  $c_{sp}$  and  $c_r$  can be regarded as grid indices in the slow time, spatial, and fast time as well. Let  $M_d = C_d$ ,  $M_{sp} = C_{sp}$ ,  $M_r = C_r$  and we have  $m_d = c_d$ ,  $m_{sp} = c_{sp}$ ,  $m_r = c_r$ . Therefore, the number of grids in the three domains can be controlled by adjusting the FFT points. As a result, we introduce the common overgridding factor

$$r_a \triangleq M_d/K = M_{sp}/L = M_r/N \geq 1. \quad (34)$$

Obviously, a higher value of  $r_a$  indicates larger number of grids in the three domains. As will be seen later in Section V, when targets are off-grid, in order to suppress high-order harmonics,  $r_a$  should be increased.

Based on the above discussion, the number of pre-detection targets satisfies  $I_{pd} \ll C_d C_{sp} C_r = M_d M_{sp} M_r$ . Since pre-detection results reveal the grid indices of the main components in the vector  $\mathbf{r}$ , we can obtain a dimension reduced model of (10) given by <sup>2</sup>

$$\mathbf{r} \approx \text{csign}(\mathbf{A}_\kappa \mathbf{x}_\kappa + \mathbf{w}). \quad (35)$$

where  $\mathbf{x}_\kappa = [x_\kappa(0), \dots, x_\kappa(i_{pd}), \dots, x_\kappa(I_{pd}-1)] \in \mathbb{C}^{I_{pd} \times 1}$ . For the  $i_{pd}$ th entry, if a target is absent,  $x_\kappa(i_{pd}) = 0$ . Otherwise,  $x_\kappa(i_{pd})$  denotes the true complex amplitude of the target whose Doppler, spatial and beat frequencies are  $f_{d,i_{pd}} = (m_{d,i_{pd}} \text{PRF})/M_d$ ,  $f_{sp,i_{pd}} = m_{sp,i_{pd}}/M_{sp}$  and  $f_{r,i_{pd}} = (m_{r,i_{pd}} f_s)/M_r$ , respectively.  $\mathbf{A}_\kappa \in \mathbb{C}^{KLN \times I_{pd}}$  is the dimension reduced observation matrix and  $\mathbf{A}_\kappa = [\mathbf{a}_\kappa(0), \dots, \mathbf{a}_\kappa(i_{pd}), \dots, \mathbf{a}_\kappa(I_{pd}-1)]$ , where  $\mathbf{a}_\kappa(i_{pd}) = \mathbf{a}_d(f_{d,i_{pd}}) \otimes \mathbf{a}_{sp}(f_{sp,i_{pd}}) \otimes \mathbf{a}_r(f_{r,i_{pd}})$ . Based on the known  $\mathbf{A}_\kappa$  and  $\mathbf{r}$ , we can try to reconstruct the vector  $\mathbf{x}_\kappa$  instead of  $\mathbf{x}$  in (10).

### B. GAMP Reconstruction

Mathematically, the goal of the target reconstruction problem is to find a sparse vector  $\mathbf{x}_\kappa$  consistent with the observation model (35). Here we recover  $\mathbf{x}_\kappa$  via Bayesian methods.

The above problem can be abstracted as a sparse signal recovery problem in generalized linear model (GLM), where a sparse signal  $\mathbf{x}_\kappa$  follows i.i.d. prior  $p(\mathbf{x}_\kappa) = \prod_{i=1}^{I_{pd}} p(x_{\kappa_i})$  and undergoes a linear transform  $\mathbf{z} = \mathbf{A}\mathbf{x}_\kappa$ , and the measurements  $\mathbf{r}$  is a componentwise probabilistic mapping of  $\mathbf{z}$ , i.e.,  $p(\mathbf{r}|\mathbf{z}) = \prod_i p(r_i|z_i)$ . To apply GAMP, the i.i.d. Bernoulli Gaussian prior distribution is imposed for the signal  $\mathbf{x}_\kappa$ , i.e.,  $p(\mathbf{x}_\kappa) = \prod_{i=1}^{I_{pd}} p(x_{\kappa_i})$

$$p(x_{\kappa_i}) = (1 - \rho_\kappa) \delta(x_{\kappa_i}) + \rho_\kappa \mathcal{CN}(x_{\kappa_i}; \mu_\kappa, \sigma_\kappa^2). \quad (36)$$

where the sparsity rate  $\rho_\kappa$ , prior nonzero mean  $\mu_\kappa$  and variance  $\sigma_\kappa^2$  are all unknown. Given that the parameters  $\boldsymbol{\theta} = [\rho_\kappa, \mu_\kappa, \sigma_\kappa^2]^T$  of the prior distribution are unknown, expectation-maximization (EM) algorithm is incorporated to iteratively learn the parameters [31]. For the details about the implementation including the EM step, please refer to [32]. Since  $\mathbf{A} \in \mathbb{C}^{KLM \times I_{pd}}$ , the computation complexity of

<sup>2</sup>Notice that for off-grid case, biases exist between the true frequencies and grids predetected. We can use 35 to represent  $\mathbf{r}$  as well. Performance of the propose target detection performance for off-grid case based on will be provide in section V.

GAMP is  $O(KLN I_{pd})$ . Without DR, GAMP works directly on the matrix  $\mathbf{A} \in \mathbb{C}^{KLM \times M_d M_{sp} M_r}$ , and the computation complexity is  $O(KLN M_d M_{sp} M_r)$ , which is significantly higher as  $I_{pd} \ll M_d M_{sp} M_r$ .

Let  $\hat{\mathbf{x}}_\kappa = [\hat{x}_\kappa(0), \dots, \hat{x}_\kappa(i_{pd}), \dots, \hat{x}_\kappa(I_{pd} - 1)]^T \in \mathbb{C}^{I_{pd} \times 1}$  denote the reconstructed vector. Based on  $\hat{\mathbf{x}}_\kappa$ , target detection can be then implemented to remove FAs in pre-detection vector  $\tilde{\mathbf{x}}_\kappa$ . Assume the detection threshold is  $\gamma_2$ . If  $|\hat{x}_\kappa(i_{pd})| \geq \gamma_2$ , a target is present in this grid. Otherwise, target is absent.

Further, to compare with the received signal before one-bit quantization, we can obtain, based on  $\hat{\mathbf{x}}_\kappa$ , the recovered synthesis signal in a vector form

$$\hat{\mathbf{s}} = \mathbf{A}_\kappa \hat{\mathbf{x}}_\kappa. \quad (37)$$

As we show later, the strength of the harmonics of the reconstructed signal  $\hat{\mathbf{s}}$  is largely reduced. It is worth noting that GAMP takes the quantization effects into consideration, and tries to find a sparse vector  $\mathbf{x}_\kappa$  while consistent with the observation model (35). As shown in [33, 34], GAMP can be viewed as the iteration between the standard linear model (SLM) running AMP and the minimum mean squared error (MMSE) or maximum a posteriori (MAP) module. The MMSE or MAP module takes the quantization into account and iteratively refine the pseudo observations of the SLM. While for the SLM, AMP takes the signal sparsity into account and estimate the signal. For the conventional FFT method, it performs directly on the binary data, which has plentiful harmonics and yields harmonic false alarms. As a result, GAMP has the powerful harmonic suppression capabilities.

### C. Considerations of Sampling Frequency

The two-stage approach combines linear and nonlinear signal processing method to implement target detection. In this paper, we consider the case that targets are sparse in the spatial, slow time and fast time domain, i.e., the number of targets  $P \ll M_d M_{sp} M_r$ . Meanwhile, we only, in general, need to take 3-order harmonics generated by targets with high received SNRs and high-order harmonics are sparse as well in the three domains. Then, the number (represented by  $Q$ ) of discrete frequencies of fundamental components and high-order harmonics satisfies  $Q \ll M_d M_{sp} M_r$  and spectrum aliasing has little impacts on target predetection. On the other hand, in order to avoid frequency ambiguities of true targets,  $f_s$  should satisfies  $f_s \geq B_r$ . Based on the above considerations, we apply Nyquist sampling frequency in this paper, i.e.,  $f_s = B_r$ <sup>3</sup>.

From the respect of nonlinear signal processing, recent works [24–27] for wireless communications study the relationship between the bound of the Fisher information and sampling frequency. It is show that

<sup>3</sup>At  $f_s = B_r$ , it will cause frequency ambiguities for high-order harmonics. However, high-order harmonics are undesired components and can be removed in the second stage.

the loss in one-bit ADC can be compensated via oversampling with respect to Nyquist rate. Nevertheless, oversampling results in noise correlation and it is hard not only to characterize the performance gain analytically, but also to design efficient algorithms. Investigating the performance gains of oversampling for one-bit radar will be left for future work.

## V. NUMERICAL RESULTS

In this section, substantial numerical experiments are provided from three aspects: Firstly, effects of one-bit quantization on target detection is evaluated. Secondly, the effectiveness of the proposed method on reconstructing of targets and suppressing FAs caused by high-order harmonics is investigated. Thirdly, the target detection performances are presented and performance comparisons are provided between one-bit radar and conventional radar using high-precision ADCs.

The variance of the additive complex noise  $2\sigma_w^2$  is assumed to be available since this information can be estimated through a training process in the built-in self-test (BIST) stage of radar. Here we set  $2\sigma_w^2 = 1$ . To perform DR-GAMP, the  $\eta$ th statistics  $x_\eta$  in (33) are set as the  $\lfloor 0.75R_d \rfloor$ th,  $\lfloor 0.75R_{sp} \rfloor$ th and  $\lfloor 0.75R_r \rfloor$ th elements of the ordered lists of reference cells in the three domains, where  $R_d$ ,  $R_{sp}$  and  $R_r$  are the corresponding numbers of reference cells. For the scale factor  $\alpha_{OS}$ , it is set according to noise false alarm  $P_{FA,w}$  and is given in the corresponding simulations.

### A. Effects of one-bit quantization on target detection

In this subsection, we firstly validate the assumption (30) via numerical experiments. Then, attenuations of 3-order harmonics relative to the fundamental frequencies, FAs caused by 3-order harmonics and SNR losses caused by one-bit quantization are discussed. After the Fourier transform, define the SNR of a fundamental frequency or a high-order harmonic in (30) as  $10\log(|A_q|^2/(2\sigma_{w_f}^2))$  dB.

1) *Validation of Noise statistical characteristics in (30)*: In (30), we assume that  $w(f)$  is Gaussian noise with its bandwidth  $B_r$ . At Nyquist sampling frequency, i.e.,  $f_s = B_r$ , the noise cells after FFT should be i.i.d. complex Gaussian random variables<sup>4</sup>. Without loss of generality, we take the fast time domain for example and consider the received one-bit signal  $v_{qC}(t)$  in (27). Assume that the number of target is  $P = 2$ . The sampling frequency is 100 MHz and the normalized frequencies of the two target are  $f_{r,1} = 0.4$  and  $f_{r,2} = 0.05$ , respectively. The observation time duration is 10 ms and the corresponding number of samples is  $N = 10^6$ .

The frequency spectrum of one-bit signal after FFT is shown in Fig. 3. It is shown that energies for both fundamental frequencies and high-order harmonics are focused in the frequency domain at

<sup>4</sup>At  $C = N$ , where  $C$  is the number of FFT point and  $N$  is the number of observations.



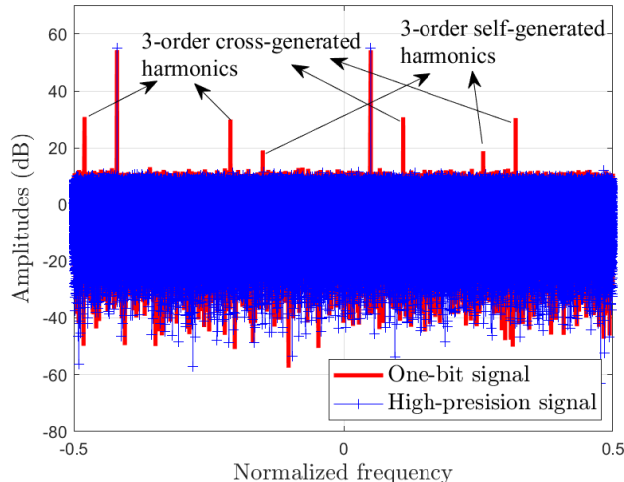


Fig. 3. Spectrums of high-precision and one-bit quantization signals. Before one-bit quantization, the received SNRs of the two targets are  $\text{SNR}_1 = \text{SNR}_2 = -5$  dB. The number of FFT points is  $C_r = 10^6$ . Note that because  $f_s = B_r$ , frequency ambiguities exist for several 3-order harmonics.

certain frequency cells. The real part of  $\mathcal{F}(v_{qC}(t))$  is, without loss of generality, considered for analyzing noise statistical characteristics. Removing cells of the fundamental frequencies and 3-order harmonics, QQplots<sup>5</sup> and autocorrelation coefficient curves are provided in Fig. 4 (a)-(d) for different received SNR cases. For the cases of  $\text{SNR} = -15$  dB and  $\text{SNR} = -5$  dB, the QQplots of the remaining cells are approximately a straight line. This means that the noise is approximately Gaussian. Nevertheless, for  $\text{SNR} = 0$  dB case, several cells with large values deviates from the straight line. The reason is that at  $\text{SNR} = 0$  dB, the 5-order harmonics can not be ignored again. If we further remove cells of 5-order harmonics, the QQplot is back to a straight line and hence, the noise is approximately Gaussian as well. Autocorrelation coefficients of noise cells are shown in Fig. 4 (d). Clearly, the noise after FFT is almost independent. Hence, the noise  $w(t)$  in (30) can be modeled as the additive Gaussian noise with the bandwidth of  $B_r$ .

2) *FAs caused by high-order harmonics*: We still consider the two targets scenario and set  $\text{SNR}_1 = \text{SNR}_2$ . The frequencies of the two targets are denotes as  $f_{r,1}$  and  $f_{r,2}$ , respectively. The attenuations of the self-generated and cross-generated 3-order harmonics relative to the fundamental frequencies are shown in Fig. 5. It can be seen that when  $\text{SNR} < -10$  dB, both the theoretical exact results (19) and (21) are consistent with their approximations (20) and (22). In addition, when  $-15 \text{ dB} \leq \text{SNR} \leq 8 \text{ dB}$ ,

<sup>5</sup>A QQplot is a visual inspection tool for checking the Gaussianity of the data. In a QQplot, deviation from a straight line is an evidence of non-Gaussianity.

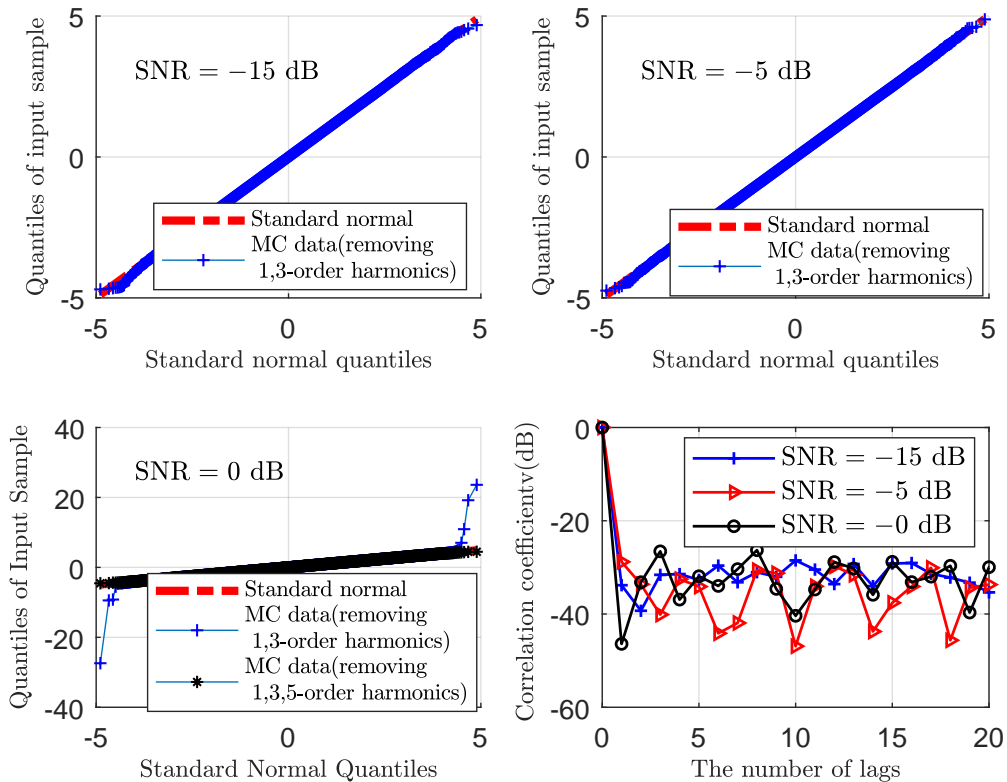


Fig. 4. QQplots and autocorrelation coefficient curves for checking the Gaussianity of data after FFT. (a) SNR = -15 dB. (b) SNR = -5 dB. (c) SNR = 0 dB. (d) Autocorrelation coefficients of noise cells for the three SNR cases.

the Monte Carlo (MC) results are consistent with (19) and (21) which validates the theoretical analysis.

In Fig. 5, it is shown that when the SNR is low, the attenuations are very large and both the self-generated and cross-generated 3-order harmonics can be ignored. As SNR increases, the attenuations becomes smaller and the strength of the 3-order harmonics can not be ignored. For example, when SNR = -5 dB, the SNRs of the 3-order cross-generated and self-generated harmonics are about 23.6 dB and 34.8 dB lower than that of fundamental frequencies, respectively. The 3-order harmonics will result in FAs in many application scenarios. Consider a set of typical parameters (details will be shown later in Table I) in automotive radar:  $K = 200$ ,  $L = 24$  and  $N = 1000$ . The digital integration gain is  $10\log(KLN) = 66.8$  dB (without considering processing loss) and after integration, the SNRs of the 3-order cross-generated and self-generated harmonics are about 38.2 dB and 27.0 dB, respectively. As a consequence, the 3-order harmonics can not be ignored. Since 3-order harmonics are target-like (as shown in Fig. 3), they will result in FAs.

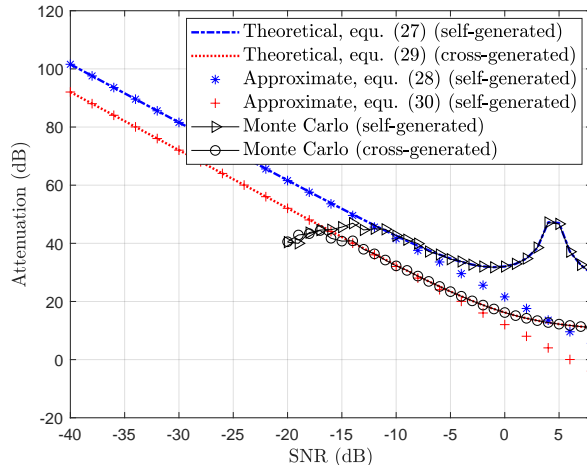


Fig. 5. Attenuations of 3-order harmonics.

Furthermore, the corresponding frequency range of 3-order harmonics is partly overlap with that of true targets (no matter how large the sampling frequency  $f_s$  is selected) and hence, linear processing methods is difficult to completely remove FAs caused by harmonics. For example, two of the 3-order harmonics that have frequencies of  $2f_{r,1} - f_{r,2}$  and  $2f_{r,2} - f_{r,1}$  may be equal to that of true targets and can not be suppressed in frequency domain <sup>6</sup>.

3) *SNR loss of one-bit quantization*: For one-bit quantization, fundamental frequencies suffer SNR losses comparing with high-precision quantization especially for scenarios with high SNR targets. The SNR loss can be evaluated through conducting statistics of the SNR differences between the conventional and one-bit radar after 3-D FFT. For a given target, the SNR loss is defined as  $\text{SNR}_c - \text{SNR}_{\text{ob}}$ , where  $\text{SNR}_c$  and  $\text{SNR}_{\text{ob}}$  denotes the target SNRs in conventional system and one-bit radar. We again consider a two targets scenario. For the first target, we fix its SNR as  $\text{SNR}_1 = -30$  dB. For the second target, its SNR is varied from  $-30$  dB to  $20$  dB. The SNR losses for the both targets are calculated and results are shown in Fig. 6. When the SNR of the second target satisfies  $\text{SNR}_2 < -10$  dB, the SNR loss is about 2 dB for both targets. As  $\text{SNR}_2$  increases from  $-10$  dB to  $20$  dB, the SNR loss of the first target increases from 2 dB to 14 dB. At  $\text{SNR}_2 = 0$  dB, the SNR loss of the first target is about 3.5 dB which is generally acceptable in practice. However, when  $\text{SNR}_2 > 12$  dB, the SNR loss of the first target is about 10 dB which can degrade the detection performance of targets with low SNRs significantly.

<sup>6</sup>The frequency locations of the 3-order harmonics of two targets are  $-3f_1, -3f_2, -2f_1 - f_2, -2f_2 - f_1, 2f_1 - f_2$  and  $2f_2 - f_1$ , respectively. In [21], oversampling are used to separate these harmonics from the fundamental frequencies. However, the last two harmonics may lie in the range of the target frequency and can not be removed via linear processing approaches.

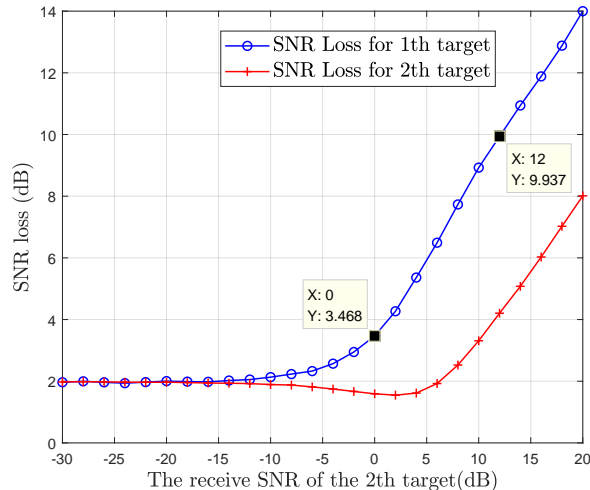


Fig. 6. SNR losses for the two targets. The blue solid line with circle marker and the red solid line with plus-sign marker denote the SNR losses for the 1th and 2th target, respectively.

The SNR losses indicate that the dynamic range is reduced for one-bit radar due to the application of one-bit quantization. A possible solution is to adopt the time varying threshold in one-bit radar system by accommodating large dynamic range of the received signal [7, 18, 35].

### B. Effectiveness of DR-GAMP

In this subsection, effectiveness of DR-GAMP is investigated under both on-grid and off-grid cases. Firstly, the benefit of DR in DR-GAMP is elucidated. Then, the excellent performance of DR-GAMP in terms of suppression of high-order harmonics is demonstrated. To evaluate the performance of reconstruction, the normalized mean squared error (NMSE)

$$\text{NMSE} = 20 \log \frac{\|\hat{\mathbf{s}} - \mathbf{A}\mathbf{x}\|_2}{\|\mathbf{A}\mathbf{x}\|_2} \quad (38)$$

is also used, where  $\hat{\mathbf{s}}$  is defined in (37).

1) *Benefit of DR*: For convenience, we still take the fast time domain for example and consider a scenario with SNRs of two targets being  $\text{SNR}_1 = \text{SNR}_2 = -5$  dB. The scale factor  $\alpha_{OS}$  of OS CFAR is set as  $\alpha_{OS} = 8.9$  dB. The number of samples is  $N = 1000$ , the bandwidth of the received signal and

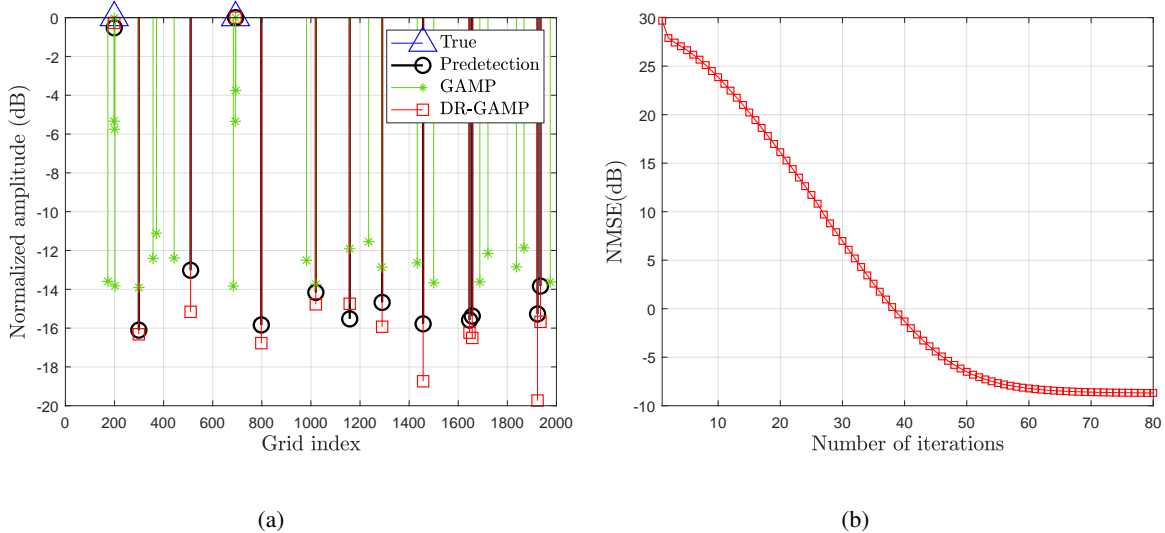


Fig. 7. The on-grid case. Fig. 7 (a) presents the normalized amplitude in frequency domain, where the normalized amplitudes are calculated such that the maximum amplitude is set as 0 dB. For GAMP, the normalized amplitude above  $-15$  dB is plotted for clarity. The maximal amplitude for the true target, predetection, GAMP and DR-GAMP results are  $-5.0$  dB,  $23.4$  dB,  $38.3$  dB,  $-5.0$  dB, respectively. Compared to GAMP, DR-GAMP recovers the amplitudes of the targets. Fig. 7 (b) presents the NMSE of DR-GAMP versus the number of iterations.

the sampling frequency are  $B_r = f_s = 100$  MHz <sup>7</sup>.

The common overgridding factor in (34) is set as  $r_a = 2$ , thus  $M_r = r_a N = 2000$  and the grid interval is  $f_s/M_r = 0.05$  MHz.

- 1) On-grid scenario: The frequencies of the two targets are  $f_{r,1} = -40.1$  MHz and  $f_{r,2} = -15.4$  MHz, respectively. The results are shown in Fig. 7. From Fig. 7 (a), several false components around true targets (their amplitudes are only  $4 \sim 6$  dB lower than the true targets) are reconstructed by GAMP, which will lead to false alarms. In contrast, DR-GAMP recovers the true targets without false components, and its NMSE is about  $-8$  dB in Fig. 7 (b), which demonstrates the benefit of DR.
- 2) Off-grid scenario: The frequencies of the two targets are  $f_{r,1} = -40.07$  MHz and  $f_{r,2} = -15.18$  MHz. The biases of the two frequencies from their nearest grids (the corresponding frequencies

<sup>7</sup>We choose  $N = 1000$  for two reasons: (1) GAMP can be directly implemented as the dimension is not huge. (2) The harmonics can be neglected and we thus focus on the benefit of dimension reduction. As shown in Fig. 5, the attenuation of the 3-order cross-generated harmonics compared to the fundamental frequency is at least 23 dB. Under one-bit quantization, Fig. 6 shows the SNR loss (corresponding to the conventional radar) is at least 2 dB. The integration gain is  $10 \log N = 30$  dB. Thus the SNR of the 3-order cross-generated harmonics is about  $-5 - 2 + 30 - 23 = 0$  dB.

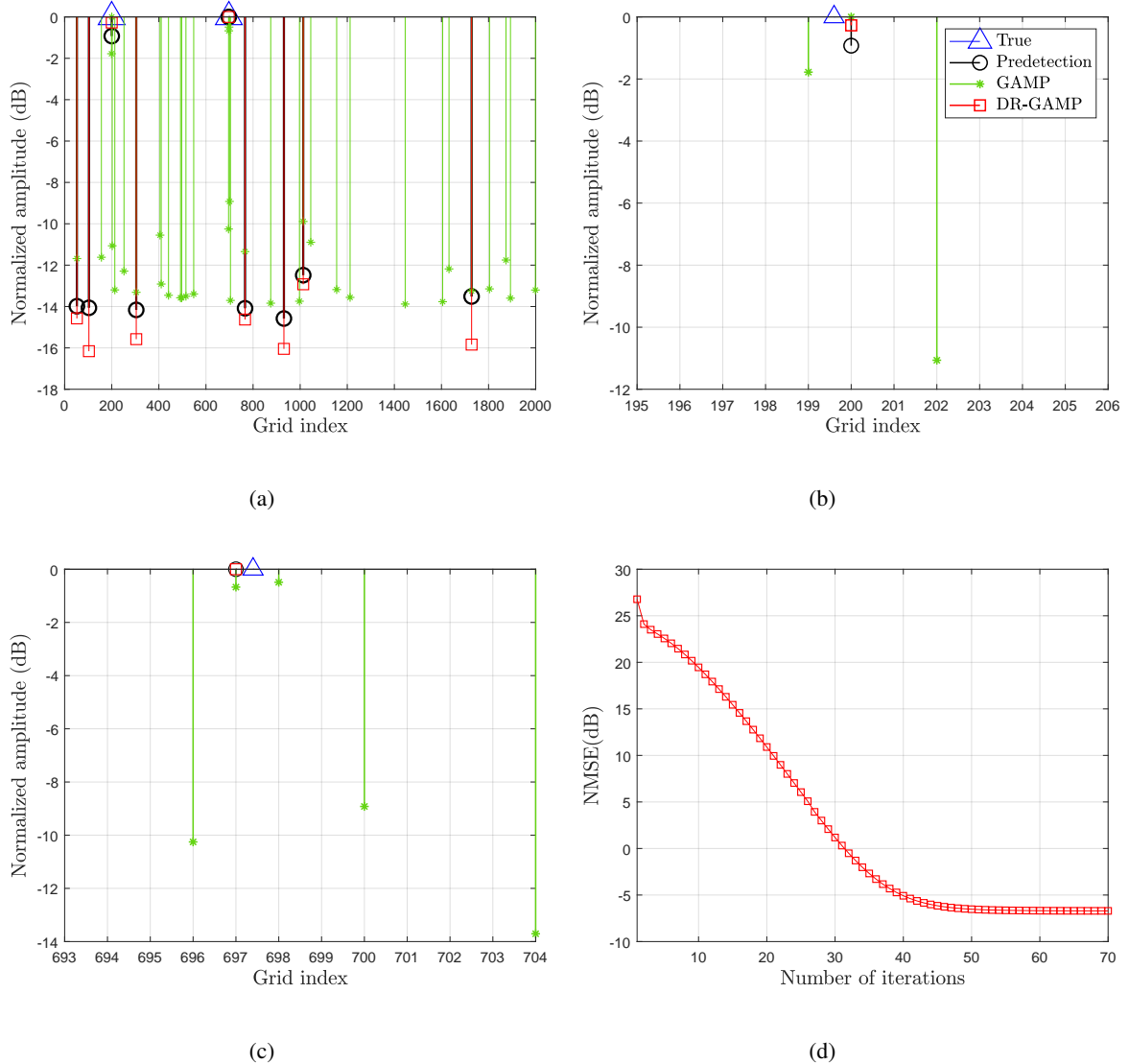


Fig. 8. The off-grid case. Fig. 8 (a) presents the normalized amplitude in frequency domain. The maximal amplitude for the true target, predetection, GAMP and DR-GAMP results are  $-5.0$  dB,  $23.2$  dB,  $38.3$  dB,  $-5.4$  dB, respectively. Compared to GAMP, DR-GAMP recovers the amplitudes of the targets. Fig. 8 (b) and (c) presents the fine details around the first and second target, respectively. Fig. 8 (d) plots the NMSE of DR-GAMP versus the number of iterations.

are  $-40.05$  MHz and  $-15.20$  MHz, respectively) are  $0.02$  MHz and  $0.02$  MHz, respectively. The results are shown in Fig. 8. The phenomenon are basically the same as that in on-grid scenario. DR-GAMP still works well and reconstructs the targets located on the grids which are nearest to the true frequencies, which also demonstrates the benefit of DR.

2) *High-order harmonic FAs suppression*: We consider the on-grid and off-grid scenarios with two targets. Simulation parameters are shown in Table I. Here we mainly concern high-order harmonic FAs

TABLE I  
SIMULATION PARAMETERS

Parameters	Value
Carrier frequency $f_c$	24GHz
Frequency modulation slope $\mu$	$10^{13}$ Hz/s
Pulse repeat interval $T_I$	$2 \times 10^{-5}$ s
Bandwidth $B_r$	100MHz
Sampling frequency $f_s$	100MHz
Number of pulses $K$	200
Number of antenna elements $L$	24
Antenna element spacing $d$	0.00625m
Number of fast time samples $N$	1000
Spatial window	Taylor
Slow time window and peak sidelobe	Chebyshev, $-60$ dB
Fast time window and peak sidelobe	Chebyshev, $-60$ dB

and set a relative high pre-detection threshold  $\alpha_{OS} = 10.6$  dB for the OS CFAR detector in the first stage. The SNR of the received signal before one-bit quantization are the same and  $\text{SNR}_1 = \text{SNR}_2 = -7$  dB.

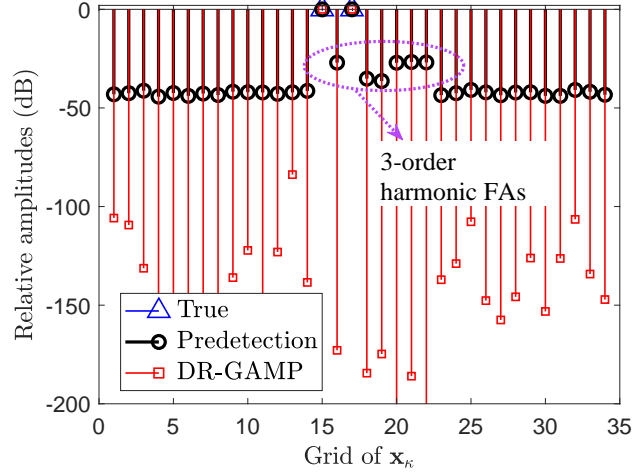
For the on-grid case, the two targets share both the same zero spatial frequencies  $f_{sp,1} = f_{sp,2} = 0$ . Beat frequencies and Doppler shifts are  $f_{r,1} = -40$  MHz,  $f_{r,2} = -3$  MHz,  $f_{d1} = 2$  KHz and  $f_{d2} = 7$  KHz, respectively. Note that the above parameter settings make the high-order harmonic FAs appear merely in the  $c_{sp}$ th spatial cell with  $f_{sp,c_{sp}} = 0$ . The overgridding factor  $r_a$  in (34) is set as  $r_a = 2$ .

For the off-grid case, targets parameters are set as follows:  $f_{d,1} = 2.1$  KHz,  $f_{d,2} = 7.35$  KHz,  $f_{sp,1} = 0.0125$  Hz,  $f_{sp,2} = 0.0354$  Hz,  $f_{r,1} = -40.015$  MHz,  $f_{r,2} = -3.06$  MHz. We investigate the performance under  $r_a = 1, 2, 3, 4$ . Under each  $r_a$ , the biases between the true frequencies of targets in the three domains and their nearest grids are given in Table II.

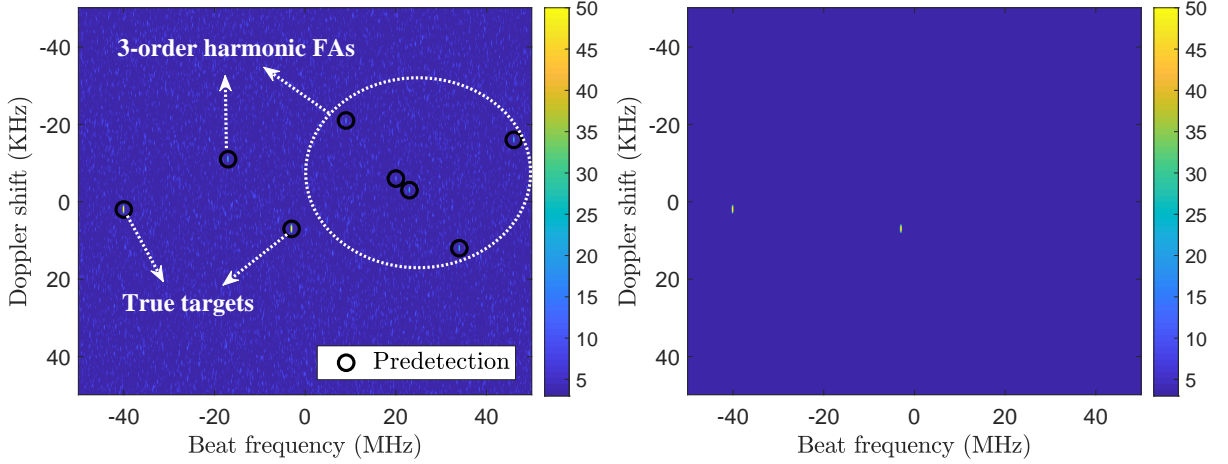
- 1) On-grid scenario: Numerical results are presented in Fig. 9. In Fig. 9(a), normalized amplitudes of vector  $\mathbf{x}_\kappa$ ,  $\tilde{\mathbf{x}}_\kappa$  and  $\hat{\mathbf{x}}_\kappa$  are presented. It can be seen that after predetection, 34 PTs are detected, including 2 true targets, 6 3-order harmonic FAs and 26 noise FAs. Then, applying the DR-GAMP algorithm, all the 3-order harmonics are suppressed significantly. Range-Doppler maps are provided in Fig. 9(b) and 9(c) for the one-bit signal and reconstructed signal at the spatial cell with  $f_{sp} = 0$ . Results show that after FFT, 3-order harmonics of one-bit signal have high SNRs, while the 3-

order harmonic strengths of the DR-GAMP reconstructed signal in (37) is negligible, which further demonstrates the excellent harmonics suppression performance of DR-GAMP.

- 2) Off-grid scenario: Simulation Results are plotted in Fig. 10. The ability of suppressing harmonics improves as  $r_a$  increases. For  $r_a = 1$ , DR-GAMP is almost ineffective to suppress harmonics. While for  $r_a = 4$ , DR-GAMP suppresses the harmonics effectively.



(a)



(b)

(c)

Fig. 9. The on-grid case. (a) Normalized amplitudes of  $\mathbf{x}_k$ ,  $\tilde{\mathbf{x}}_k$  and  $\hat{\mathbf{x}}_k$ . The maximal amplitudes for the true target, predetection and DR-GAMP results are  $-7.0$  dB,  $55.4$  dB and  $-7.0$  dB, respectively. (c) Pre-detection results on the range-Doppler map (one-bit data after FFT) at the spatial cell with  $f_{sp} = 0$ . (d) Reconstructed range-Doppler map (based on the reconstructed signal in (37) to perform FFT) at the spatial cell with  $f_{sp} = 0$ .



TABLE II  
PARAMETER SETTINGS FOR THE OFF-GIRD CASE.

$r_a$	PRF/ $M_d$ (KHz)	$1/M_{sp}$ (Hz)	$f_s/M_r$ (MHz)	$\Delta f_{d,1}$ (KHz)	$\Delta f_{d,2}$ (KHz)	$\Delta f_{sp,1}$ (Hz)	$\Delta f_{sp,2}$ (Hz)	$\Delta f_{r,1}$ (MHz)	$\Delta f_{r,2}$ (MHz)
1	0.5	0.0417	0.1	0.1	0.15	0.0125	0.0063	0.015	0.04
2	0.25	0.0208	0.05	0.1	0.1	0.0083	0.0063	0.015	0.01
3	0.167	0.139	0.033	0.067	0.0167	0.0014	0.0063	0.015	0.0067
4	0.125	0.0104	0.025	0.025	0.025	0.0021	0.0042	0.01	0.01

<sup>1</sup>  $\Delta f$  denote the bias between the true frequency and its nearest grid.

### C. Performance comparisons between one-bit and conventional radar

In this subsection, the detection performance of one-bit radar is compared with that of the conventional radar under off-grid case. Two scenarios are considered:

- Scenario 1: 10 targets with identical SNRs are added for each trial. The SNRs of targets varies from  $-28$  dB to  $-19$  dB.
- Scenario 2: The parameters are the same as scenario 1, except that we add a new target with a high SNR being 0 dB.

For each trial, all targets are randomly added in the spatial, slow time, and fast time domain. The number of MC trials is 100. The number of pulses, antenna elements, samples in the fast time domain are  $K = 100$ ,  $L = 10$  and  $N = 100$ . When 3-D FFT is implemented, data windows are used for both conventional and one-bit radar prior to 3-D FFT processing to suppress the sidelobe of strong targets. For slow time and fast time domain, Chebyshev window is adopted with peak sidelobe of  $-40$  dB. In the spatial domain, we adopt the Taylor window. The SNR loss caused by data windows in the three domains is about 2.8 dB [30, pp. 257].

For one-bit radar, the overgridding factor is  $r_a = 4$ . The threshold  $\gamma_1$  in (33) is  $\alpha_{OS} = 7.0$  dB <sup>8</sup> and  $\eta$  are 18, 75 and 75 in spatial, slow time, and fast time domain, respectively. To detect targets based on reconstructed results in the second stage, the threshold  $\gamma_2$  should be chosen carefully. If  $\gamma_2$  is too large, the true targets can be missed. While if  $\gamma_2$  is too small, the FA rate increases. In this paper, we empirically set  $\gamma_2 = (G_a - 11.6)$  dB, where  $G_a = 10\log(KLN)$ .

For the conventional radar, 3-D FFT and OS CFAR detector is implemented to detect targets. The parameter settings about the OS CFAR are the same as the one-bit radar except the scale factor  $\alpha_{OS}$ , which is set based on the average FA rate of the one-bit radar. The detection performances of the two

<sup>8</sup>Since the predetection in the first stage only provides coarse information about targets and the GAMP algorithm is powerful to suppress FAs, we can, in the first stage, set a lower threshold than that of conventional system.

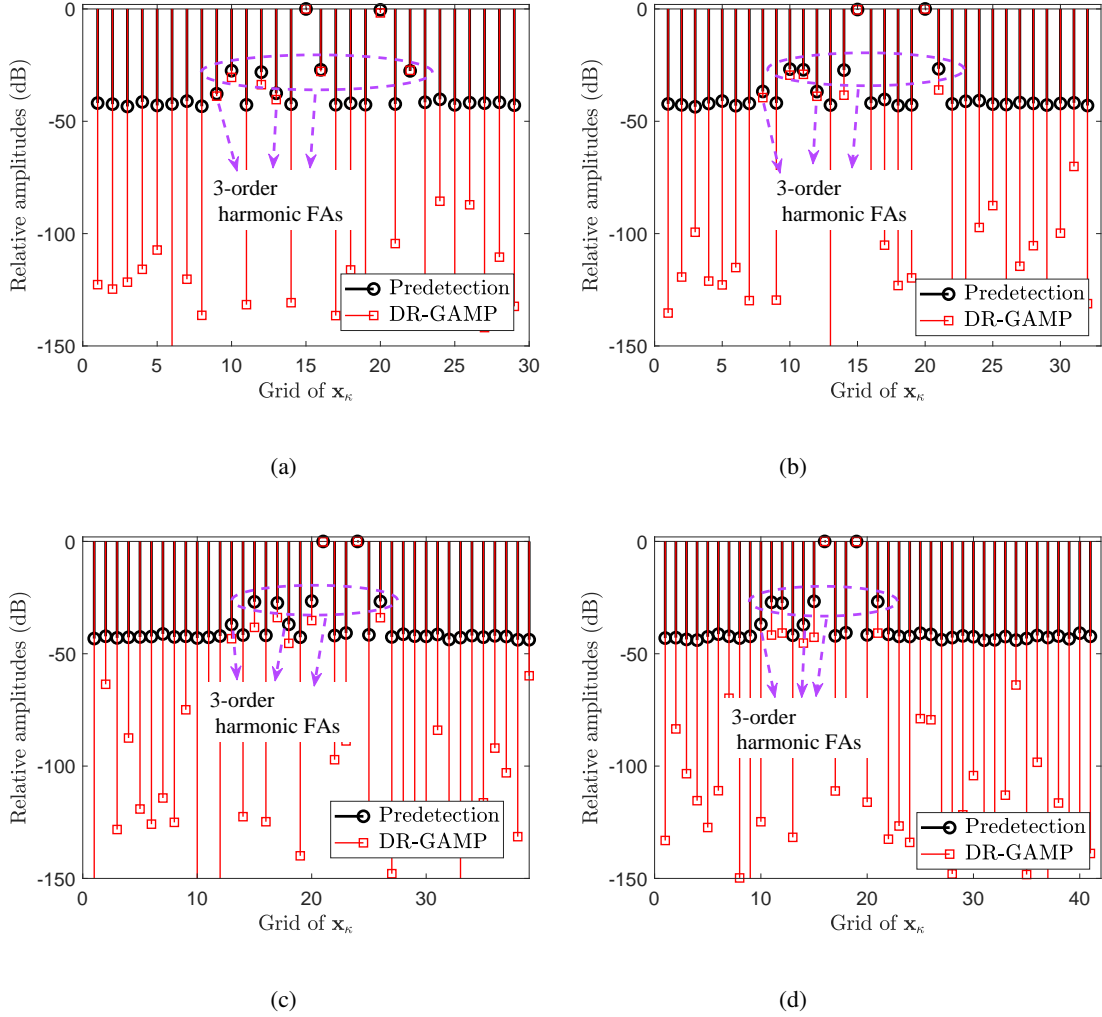


Fig. 10. Off-grid case. Fig. 10(a), 10(b), 10(c) and 10(d) present the normalized amplitudes of  $\tilde{x}_{\kappa}$  and  $\hat{x}_{\kappa}$  corresponding to  $r_a = 1, 2, 3, 4$ . The maximal amplitudes for the predetection and DR-GAMP results are 54.2 dB and  $-9.9$  dB ( $r_a = 1$ ), 54.9 dB and  $-8.4$  dB ( $r_a = 2$ ), 55.1 dB and  $-7.6$  dB ( $r_a = 3$ ), 55.2 dB and  $-7.3$  dB ( $r_a = 4$ ).

system are compared under the same FA rate. For the first scenario, the average FA rates of one-bit radar are  $P_{FA,1} = 7.2 \times 10^{-5}$  and we set the scale factor in the conventional radar as  $\alpha_{OS,c1} = 9.9$  dB. For the second scenario, the average FA rates of one-bit radar are  $P_{FA,2} = 3.5 \times 10^{-4}$  and we set  $\alpha_{OS,c2} = 8.9$  dB.

The detection performances versus the target SNRs for both scenarios are presented in Fig. 11(a) and Fig. 11(b). For the first scenario, though SNR loss of targets is 2 dB, the performance of one-bit radar has a slight superiority to the conventional system, as shown in Fig. 11(a). At  $P_D = 0.5$ , the performance gain is about 0.5 dB. The reason is that there exists 2.8 dB weighted loss in the conventional radar

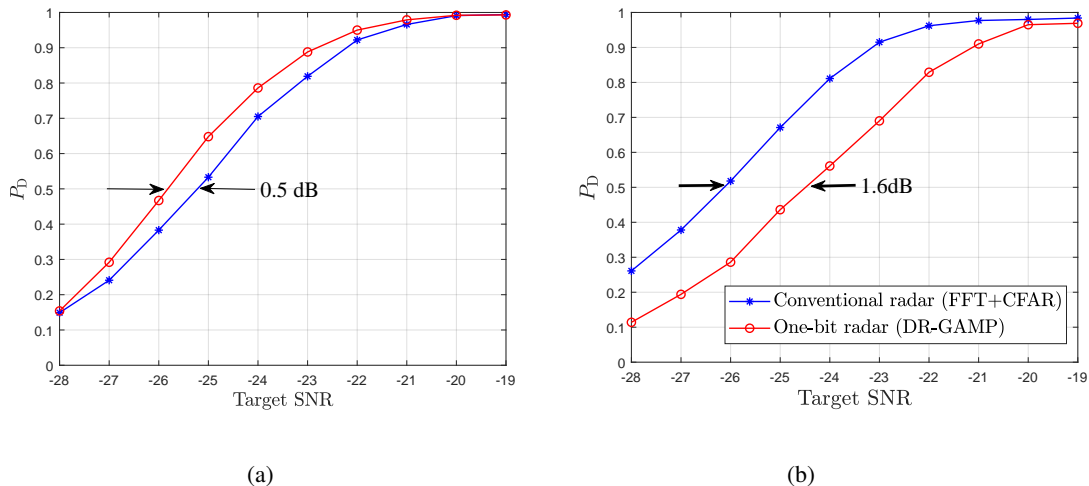


Fig. 11. Performance comparisons. (a) Scenario 1: Low received SNRs case. (b) Scenario 2: With an additional high SNR target case. Note that  $P_D$  is calculated as the detection probability of targets with low SNRs varying from  $-28$  dB to  $-19$  dB, and the target with SNR = 0 dB is removed.

system. In contrast, for the one-bit radar, although the weighted loss still exists in the first predetection stage, a lower threshold  $\gamma_1 < \gamma_c$  is set to have a higher sensitivity, and in the second stage, GAMP algorithm which has no weighted loss is applied to suppress FAs.

For the second scenario, due to the presence of the target with high received SNR, SNR loss of weak targets increases from 2 dB to 3.5 dB (refer to Fig. 5) and this makes the one-bit system inferior to the conventional system. At  $P_D = 0.5$ , the one-bit system has about 1.6 dB performance loss under the parameter settings.

## VI. CONCLUSIONS

In this paper, we investigate problems encountered in one-bit LFM CW radar and propose a two-stage DR-GAMP approach for target detection. It is shown that for a multiple targets scenarios, the 3-order harmonics including self-generated and cross-generated terms can not be omitted and linear processing is ineffective because it can not suppress these 3-order harmonics especially for 3-order cross-generated terms. As a result, a two stage DR-GAMP target detection approach is proposed. In the first stage, the linear preprocessing is performed to coherently integrate the received data and then, CFAR is performed to predetect the targets. Based on CFAR results, the number of grids in the target space is reduced significantly. Then, the GAMP algorithm is proposed to reconstruct true targets. Substantial numerical experiments are conducted to validate the effectiveness of DR-GAMP.

## VII. APPENDIX

## A. The average amplitudes of harmonics

The average of  $v_q(t)$  with respect to  $w(t)$  is given by (13).

For  $m = 0$ , its average coefficient  $c_0$  is

$$c_0 = -\frac{j}{\pi} \int_{-\infty}^{\infty} \frac{\exp\left(-\frac{\sigma_w^2 \xi^2}{2}\right)}{\xi} \prod_{p=1}^P J_0(\xi A_p) d\xi \quad (39)$$

For the first kind Bessel function, we have  $J_m(x) = J_m(-x)$  for  $m$  being even, otherwise  $J_m(x) = -J_m(-x)$ . As a consequence, we have

$$c_0 = 0. \quad (40)$$

Similarly, for the self-generated even harmonics, its average amplitudes are zeroes as well. For the odd harmonics, we calculate the case where  $P = 2$ . For general  $P$ , calculations are very similar but the analytical expressions are hard to obtain.

For  $P = 2$ , two equations [36, pp. 1096, 6.633, eq.(1)] and [36, pp. 1097, 6.633, eq.(5)] are utilized. Without loss of generality, we calculate the coefficient of the  $m$ -order self-generated harmonics  $c_{m,0} \cos(m\omega_1 t + m\Phi_1)$  from the first target signal  $A_1 \cos(\omega_1 t + \Phi_1)$ . The coefficient can be calculated as

$$\begin{aligned} c_{m,0} &= -\frac{2j^{m+1}}{\pi} \int_{-\infty}^{\infty} \frac{\exp\left(-\frac{\sigma_w^2 \xi^2}{2}\right)}{\xi} J_0(A_2 \xi) J_m(A_1 \xi) d\xi \\ &= -\frac{4j^{m+1}}{\pi} \frac{A_1^m \left(\frac{\sigma_w^2}{2}\right)^{-\frac{m}{2}}}{2^{m+1} \Gamma(m+1)} \sum_{i=0}^{\infty} \frac{\Gamma(i + \frac{m}{2})}{i! \Gamma(i+1)} \left(-\frac{A_2^2}{2\sigma_w^2}\right)^i \times F\left(-i, -i; m+1; \frac{A_1^2}{A_2^2}\right). \end{aligned} \quad (41)$$

If  $A_1 = A_2$ , (41) can be further simplified as

$$\begin{aligned} c_{m,0} &= -\frac{2j^{m+1}}{\pi} \int_{-\infty}^{\infty} \frac{\exp\left(-\frac{\sigma_w^2 \xi^2}{2}\right)}{\xi} J_0(A_2 \xi) J_m(A_1 \xi) d\xi \\ &= -j^{m+1} \sqrt{\frac{2}{\pi}} \frac{1}{\left(\frac{m-1}{2}\right)! m} 2^{-\frac{3(m-1)}{2}} {}_3F_3\left(\frac{m+1}{2}, \frac{m}{2} + 1, \frac{m}{2}; 1, m+1, m+1; -\frac{2A_2^2}{\sigma_w^2}\right). \end{aligned} \quad (42)$$

For the  $m$ -order cross-generated harmonics  $c_{m_1, m_2} \cos(m_2 \omega_2 t + m_2 \Phi_2) \cos(m_1 \omega_1 t + m_1 \Phi_1)$  where  $m = m_1 + m_2$  ( $m_1, m_2 \geq 1$ ), its coefficient can be calculated as

$$\begin{aligned} c_{m_1, m_2} &= -\frac{4j^{m+1}}{\pi} \int_{-\infty}^{\infty} \frac{\exp\left(-\frac{\sigma_w^2 \xi^2}{2}\right)}{\xi} J_{m_2}(A_2 \xi) J_{m_1}(A_1 \xi) d\xi, \\ &= -\frac{8j^{m+1}}{\pi} \frac{A_1^{m_1} A_2^{m_2} \left(\frac{\sigma_w^2}{2}\right)^{-\frac{m}{2}}}{2^{m+1} \Gamma(m_1+1)} \sum_{i=0}^{\infty} \frac{\Gamma(i + \frac{m}{2})}{i! \Gamma(i + m_2 + 1)} \left(-\frac{A_2^2}{2\sigma_w^2}\right)^i \times F\left(-i, -m_2 - i; m_1 + 1; \frac{A_1^2}{A_2^2}\right). \end{aligned} \quad (43)$$

When  $A_1 = A_2$ , we have

$$\begin{aligned}
c_{m_1, m_2} &= -\frac{4j^{m+1}}{\pi} \int_{-\infty}^{\infty} \frac{\exp\left(-\frac{\sigma_w^2 \xi^2}{2}\right)}{\xi} J_{m_2}(A_2 \xi) J_{m_1}(A_1 \xi) d\xi \\
&= -j^{m+1} \sqrt{\frac{2}{\pi}} 2^{-m+2} \frac{(m-2)!!}{m_1! m_2!} \left(\frac{A_1}{\sigma_w}\right)^m {}_3F_3\left(\frac{m+1}{2}, \frac{m}{2}+1, \frac{m}{2}; m_2+1, m_1+1, m+1; -\frac{2A_1^2}{\sigma_w^2}\right). \quad (44)
\end{aligned}$$

#### REFERENCES

- [1] P. Ghelfi, F. Laghezza, F. Scotti, et. al., “A fully photonics-based coherent radar system” *Nature*, vol. 507, no. 7492, pp. 341-345, 2014.
- [2] E. Baransky, G. Itzhak, N. Wagner, I. Shmuel, E. Shoshan, and Y. Eldar, “Sub-Nyquist radar prototype: Hardware and algorithm” *IEEE Trans. Aerosp. Electron. Syst.*, vol. 50, no. 2, pp. 809-822, 2014.
- [3] L. Wang, Y. Guo, P. Li, T. Zhao and Y. Wang, “White-chaos radar with enhanced range resolution and anti-jamming capability,” *IEEE Photon. Technol. Lett.*, vol. 29, no. 20, pp. 1723-1726, 2017.
- [4] K. Eldhuset, “High-resolution spaceborne SAR processing using the decomposed transfer function,” *IEEE Trans. Aerosp. Electron. Syst.*, vol. 53, no. 5, pp. 2187-2198, 2017.
- [5] B. Le, T. Rondeau, J. Reed, C. Bostian, “Analog-to-digital converters,” *IEEE Signal Process. Mag.*, vol. 22, no. 6, pp. 69-77, 2005.
- [6] A. Ali, and W. Hamouda, “Low power wideband sensing for one-bit quantized cognitive radio systems,” *IEEE Wireless Commun. Lett.*, vol. 5, no. 1, pp. 16-19, 2016.
- [7] J. Li, M. M. Naghsh, S. J. Zahabi and M. M. Hashemi, “Compressive radar sensing via one-bit sampling with time-varying thresholds,” *50th Asilomar Conference on Signals, Systems and Computers*. Pacific Grove, CA, USA, pp. 1164-1168, 2016.
- [8] J. Ren and J. Li, “One-bit digital radar,” *51st Asilomar Conference on Signals, Systems, and Computers*, Pacific Grove, CA, USA, pp. 1142-1146, 2017.
- [9] S. M. Patole, M. Torlak, D. Wang and M. Ali, “Automotive radars: A review of signal processing techniques,” *IEEE Signal Process. Mag.*, vol. 34, no. 2, pp. 22-35, 2017.
- [10] J. Lien, N. Gillian, M. E. Karagozler, P. Amihoud, C. Schwesig, E. Olson, H. Raja and I. Poupyrev, “Soli: Ubiquitous gesture sensing with millimeter wave radar,” *ACM Trans. Graph.*, vol. 35, no. 4, pp. 142:1-142:19, 2016.
- [11] Y. Jeon, N. Lee, S. Hong and R. W. Heath, “One-bit sphere decoding for uplink massive MIMO systems with one-bit ADCs,” *IEEE Trans. Wireless Commun.*, vol. 17, no. 7, pp. 4509-4521, 2018.
- [12] Z. Liu, C. Li and Z. Zhang, “One-Bit Recursive Least-Squares Algorithm with Application to Target Localization,” *IEEE Trans. Aerosp. Electron. Syst.*, Early Access, pp. 1-16, 2018.

- [13] C. Mollén, J. Choi, E. G. Larsson, and R. W. Heath, “Uplink performance of wideband massive MIMO with one-bit ADCs,” *IEEE Trans. Wireless Commun.*, vol. 16, no. 1, pp. 87-100, 2017.
- [14] J. Mo and R. W. Heath, “Capacity analysis of one-bit quantized MIMO systems with transmitter channel state information,” *IEEE Trans. Signal Process.*, vol. 63, no. 20, pp. 5498-5512, 2015.
- [15] J. Fang, and H. Li, “Adaptive distributed estimation of signal power from one-bit quantized data,” *IEEE Trans. Aerosp. Electron. Syst.*, vol. 46, no. 4, pp. 1893-1905, 2010.
- [16] T. Feuillen, C. Xu, L. Vandendorpe and L. Jacques, “1-bit localization scheme for radar using dithered quantized compressed sensing,” *arXiv*. Available: <https://www.researchgate.net/publication/325778565>, 2018.
- [17] O. Bjorndal, Single bit radar systems for digital integration, PhD (thesis), 2017.
- [18] B. Zhao, L. Huang, J. Li, M. Liu and J. Wang, “Deceptive SAR jamming based on 1-bit sampling and time-varying thresholds,” *IEEE J. Sel. Topics Appl. Earth Observ.*, vol. 11, no. 3, pp. 939-950, 2018.
- [19] F. Franceschetti, V. Pascazio and G. Schirinzi, “Processing of signum coded SAR signal: theory and experiments,” *IEE Proceedings F - Radar and Signal Processing*, vol. 138, no. 3, pp. 192-198, 1991.
- [20] G. Fornaro, V. Pascazio and G. Schirinzi, “Synthetic aperture radar interferometry using one bit coded raw and reference signals,” *IEEE Trans. Geosci. Remote Sens.*, vol. 35, no. 5, pp. 1245-1253, 1997.
- [21] V. Pascazio, G. Schirinzi, “Synthetic aperture radar imaging by one bit coded signals,” *Electron. Commun. Eng. Journal*, vol. 10, no. 1, pp. 17-28, 1998.
- [22] S. R. Axelsson, “Noise Radar for range/Doppler processing and digital beamforming using low-bit ADC,” *IEEE Trans. Geosci. Remote Sens.*, vol. 41, no. 12, pp. 2703-2720, 2003.
- [23] X. Dong, Y. Zhang, “A MAP approach for 1-bit compressive sensing in synthetic aperture radar imaging,” *IEEE Geosci. Remote Sens. Lett.*, vol. 12, no. 6, pp. 1237-1241, 2015.
- [24] M. Stein, A. Mezghani, and J. A. Nossek, “A lower bound for the Fisher information measure,” *IEEE Signal Process. Lett.*, vol. 21, no. 7, pp. 796-799, Jul. 2014.
- [25] M. Schluter, M. Dörpinghaus, G. P. Fettweis, “Bounds on channel parameter estimation with 1-Bit quantization and oversampling,” *IEEE 19th International Workshop on Signal Processing Advances in Wireless Communications (SPAWC)*, Kalamata, pp. 1-5, 2018.
- [26] A. B. Üçüncü, A. Ö. Yılmaz, “Oversampling in one-bit quantized massive MIMO systems and performance analysis,” *IEEE Trans. Wireless Commun.*, vol. 17, no. 12, pp. 7952-7964, 2018.
- [27] S. Bender, L. Landau, M. Dörpinghaus, G. Fettweis, “Communication with 1-bit quantization and

- oversampling at the receiver: Spectral constrained waveform optimization,” *IEEE 17th International Workshop on Signal Processing Advances in Wireless Communications (SPAWC)*, Edinburgh, pp. 1-5, 2016.
- [28] Y. Chi, L. L. Scharf, A. Pezeshki and A. R. Calderbank, “Sensitivity to basis mismatch in compressed sensing,” *IEEE Trans. Signal Process.*, vol. 59, no. 5, May 2011.
- [29] A. Milton and I. Stegun, *Handbook of Mathematical Functions with Formulas, Graphs, and Mathematical Tables*. Dover Publications, 1970.
- [30] M. A., Richards, *Fundamentals of Radar Signal Processing*. New York: McGraw-Hill, 2005.
- [31] J. Vila and P. Schniter, “Expectation-maximization Gaussian-mixture approximate message passing,” *IEEE Trans. on Signal Process.*, vol. 61, no. 19, pp. 4658-4672, 2013.
- [32] H. Cao, J. Zhu, J and Z. Xu, “Adaptive one-bit quantization via approximate message passing with nearest neighbour sparsity pattern learning,” *IET Signal Process.*, vol. 12, no. 5, pp. 629-635, 2018.
- [33] X. Meng, S. Wu, S. and J. Zhu, “A unified Bayesian inference framework for generalized linear model,” *IEEE Signal Process. Lett.*, vol. 25, no. 3, pp. 398-402, 2018.
- [34] J. Zhu, “A comment on the “A unified Bayesian inference framework for generalized linear models”,” technical note, arXiv:1904.04485.
- [35] F. Liu, H. Zhu, J. Li, P. Wang, P. V. Orlik, “Massive MIMO channel estimation using signed measurements with antenna-varying threshold,” *IEEE Statistical Signal Processing Workshop*, July 11, pp. 188-192, 2018.
- [36] I. Gradshteyn and I. Ryzhik, “Tables of integrals, series, and products,” *American Journal of Physics*, vol. 56, no. 10, pp. 958-958, 1988.